1290

UNIVERSIDADE Ð
COIMBRA

David José Simões Pereira

MODELAÇÃO MATEMÁTICA E EXPERIMENTAL DE UMA BARREIRA ANTI-FOGO

VOLUME 1

Dissertação no âmbito do Mestrado Integrado em Engenharia Mecânica na Especialidade de Energia e Ambiente orientada pelo Professor Doutor Miguel Rosa Oliveira Panão e Professor Doutor Carlos Xavier Pais Viegas e apresentada ao Departamento de Engenharia Mecânica da Faculdade de Ciências e Tecnologia da Universidade de Coimbra

Outubro de 2020

1 2 9 0

FACULDADE DE
CIÊNCIAS E TECNOLOGIA
UNIVERSIDADE DE
COIMBRA

Mathematical and experimental modelling of a fire-proof barrier

Submitted in Partial Fulfilment of the Requirements for the Degree of Master in Mechanical Engineering in the speciality of Energy and Environment

Modelação matemática e experimental de uma barreira anti-fogo

Author
David José Simões Pereira

Advisors
Miguel Rosa Oliveira Panão
Carlos Xavier Pais Viegas

Jury

President	**Professor Doutor Manuel Carlos Gameiro da Silva** **Professor Catedrático da Universidade de Coimbra**
Vowels	**Professor Doutor José Joaquim da Costa** **Professor Auxiliar da Universidade de Coimbra** **Professor Doutor Jorge Rafael Nogueira Raposo** **Professor Auxiliar Convidado da Universidade de Coimbra**
Advisor	**Professor Doutor Miguel Rosa Oliveira Panão** **Professor Auxiliar da Universidade de Coimbra**

Institutional Collaboration

Associação para o
Desenvolvimento da
Aerodinâmica
Industrial

Centro de Estudos
sobre Incêndios
Florestais

Coimbra, October, 2020

"Do not go where the path may lead,
go instead where there is no path and leave a trail."
Ralph Waldo Emerson

À família e amigos.

Agradecimentos

A realização deste trabalho só foi conseguida devido ao apoio incondicional de algumas pessoas às quais dedico umas palavras de agradecimento. Aos meus orientadores, Miguel Panão e Carlos Viegas, pelas críticas construtivas que cultivaram a minha aprendizagem, pela transmissão de conhecimentos em períodos chave e pela orientação imprescindível aquando da elaboração da dissertação. Ao Samuel e a todos os membros do ADAI, pelo apoio e ajuda em momentos essenciais. À minha família por todo o apoio nos últimos anos, por todo o carinho e compreensão que sempre tiveram comigo. À Isa, a minha eterna mentora, por ter estado sempre presente desde os meus primeiros passos na Universidade, por me guiar e apoiar ao longo dos últimos anos. Ao Eduardo, por todos os anos de amizade e companheirismo. A todo o meu grupo de amigos, por estarem sempre presentes, mesmo com a distância imposta, por todas as conversas e gargalhadas, por todas as partilhas e trocas de ideias. Ao ISEC por partilhar material essencial à execução da dissertação. A todos os amigos, colegas e professores que contribuíram de alguma forma para o meu percurso académico, um muito obrigado.

Resumo

Ano após ano, Portugal enfrenta épocas de incêndios florestais com consequências devastadoras. Para além da queima de milhares de hectares de floresta, os fogos florestais levam à destruição de estruturas e à perda de vidas humanas. Muitos estudos revelam que esta catástrofe natural é uma ameaça crescente. Logo, torna-se imperativo desenvolver soluções mais eficazes para a proteção de pessoas e estruturas, como a barreira anti-fogo que é estudada nesta tese. Este trabalho teve como foco o comportamento térmico de uma barreira de fibra de vidro revestida com alumínio quando exposta a uma fonte de calor que varia com o tempo.

Inicialmente foi feito um estudo do estado de arte de modelos térmicos para barreiras anti-fogo. Contudo, nenhum dos modelos analisados se revelou aplicável à barreira em estudo. Muitos modelos só são aplicáveis a barreiras com elevada condutibilidade térmica (barreiras metálicas) em que se considera que há uniformização da distribuição da temperatura ao longo da sua espessura na sua evolução temporal.

Face a esta necessidade foi desenvolvido um novo modelo semi-analítico aplicável à situação em estudo. A precisão do modelo foi aferida comparando as suas previsões com experiências laboratoriais utilizando uma fonte de calor convectiva. Os resultados das experiências mostraram uma boa aproximação entre os valores medidos e as previsões obtidas pelo modelo.

No futuro, este modelo deve ser melhorado de modo a incluir sistemas de arrefecimento a água que não foram considerados no presente trabalho. Isso permitirá otimizar o consumo de água enquanto se conserva a integridade da barreira ao longo de toda a exposição a uma fonte de calor de elevada intensidade.

Palavras Chave: Incêndios florestais, Barreira anti-fogo, Temperatura, Fluxo de calor, Função de transferência

Abstract

Year after year, Portugal faces wild fire seasons with devastating consequences. Besides burning thousands of hectares of forest, wildfires lead to the destruction of structures and the loss of human lives. Several studies evidence how this natural catastrophe is an increasing threat. Consequently, it is imperative to develop more effective solutions to protect people and structures, such as the fire-proof barrier investigated in this thesis. The work focuses on the thermal behaviour of a fibreglass barrier with an aluminium coating while being exposed to a transient heat source.

Initially, the state-of-the-art for fire-proof barrier models showed that none of the analyzed models was applicable to this barrier. Many of the already existing models are only applicable to barriers with high thermal conductivity (metallic barriers), considering a uniform temperature distribution, being only a function of time.

Due to the lack of an existing model for this case, this dissertation presents the development of a new semi-analytical transient heat transfer model for coated thermal fireproof barriers. The accuracy of the model was evaluated by comparing its predictions with laboratory experiments using a convective heat source. The experimental results showed a good approximation between the measured values and the model's predictions. In the future, improvement in the model should include water cooling systems that were not considered in this work. The purpose is to allow an optimization of water consumption while conserving the barrier's integrity throughout the exposure to a high intensity heat source.

Keywords: Wild fires, Fire-proof barrier, Temperature, Heat flux, Transfer function

Contents

List of Figures **v**

List of Tables **vii**

Nomenclature **ix**

1 Introduction **1**

1.1 Literature Review 2

1.2 Objectives 7

2 Coated thermal barrier heat transfer model **9**

2.1 Theoretical Testing of the heat transfer model 15

2.2 Improved approximation for the barrier's backside thermal behaviour . 18

3 Experimental Setup for heat transfer model validation **21**

3.1 Model changes to account for experimental conditions 23

3.2 Application of the model modified for the experimental setup 24

4 Results and Discussion **27**

5 Conclusions **35**

Bibliography **37**

Appendix A **39**

Appendix B **43**

Procedure to determine the barrier's thermal conductivity: 43

Procedure to measure barrier response to convective heat flux: 43

List of Figures

Figure 1.1 Number of fires, per decade and country 1

Figure 1.2 Burnt area (ha), per decade and country. 2

Figure 1.3 General barrier description 3

Figure 1.4 Experimental setup used by Meredith *et al.* (2013) 3

Figure 1.5 Experimental setup used by Lev & Strachan (1989) 4

Figure 1.6 Experimental setup used by Hsu *et al.* (2011). 6

Figure 1.7 Fire blanket model by Hsu *et al.* (2011). 6

Figure 2.1 Schematic of the fiberglass coated with aluminum. 9

Figure 2.2 Exact transfer function (gray) and steady-state transfer function (black) (For Bi $= 1$, $C^*_{t,f} = 0.5$ and $\zeta = 0.5$). 13

Figure 2.3 Exact transfer function (dark grey), Approximate function (light grey) and Quasi-static function (black) (For Bi $= 1$, $C^*_{t,f} = 0.5$ and $\zeta = 0.5$). 14

Figure 2.4 Average error and maximum error percentage evolution relative to mesh 4 (For Bi $= 1$, $C^*_{t,f} = 0.5$ and $\phi_h = 100°C$). 16

Figure 2.5 Approximate solution (blue) and reference solution (red) (For Bi $= 1$, $C^*_{t,f} = 0.5$ and $\phi_h = 100°C$). 17

Figure 2.6 Approximate solution (blue) and reference solution (red) (For Fo$_{max} = 10$, Bi $= 1$ and $C^*_{t,f} = 0.5$). 17

Figure 2.7 Approximate solution (blue) and reference solution (red) (For Fo$_{max} = 2$, Bi $= 1$ and $C^*_{t,f} = 0.5$). 18

Figure 2.8 1st order Approximate solution (blue), 2nd order Approximate solution (red) and reference solution (black) (For Bi $= 1$, $C^*_{t,f} = 0.5$ and $\phi_h = 100°C$). 19

Figure 3.1 Illustration of the experimental setup built to validate the heat transfer model. 22
Figure 3.2 Experimental Setup to determine k_{fg} 22

Figure 4.1 Unprocessed experimental data 27
Figure 4.2 Incident hot air temperature. 28
Figure 4.3 Front temperature evolution of the barrier. 29
Figure 4.4 Model's prediction error in front side temperature 29
Figure 4.5 Back temperature evolution of the barrier. 30
Figure 4.6 Model's prediction error in back side temperature. 30
Figure 4.7 Heat flux evolution with time. 31
Figure 4.8 Simplified representation of the thermocouple installation. . . . 32
Figure 4.9 System M electrical analog. 32
Figure 4.10 System E electrical analog. 32
Figure 4.11 Simulated temperature evolution. 34

Figure 1 Exact transfer function (black), $F_{1sOS}(s \to 0)$ transfer function (dark grey) and $F_{1sOS}(s \to \infty)$ transfer function (light grey) (For $K = 2$ and $\tau = 3$). 40
Figure 2 Response to a unitary step input function for all transfer functions (For K=2 and $\tau = 3$). 40
Figure 3 Response to a ramp input function (slope=1) for all transfer functions (For K=2 and $\tau = 3$). 41
Figure 4 Front-side of barrier 44
Figure 5 Back side of barrier 45
Figure 6 Front side of barrier 46

List of Tables

Table 2.1 Mesh information. 15

Table 3.1 Thermal and geometric properties of the thermal barrier's materials. 23

Table 3.2 New constants of the modified model to include the aluminium tape used to attach thermocouples in the experimental setup. 24

Table 4.1 Electrical analogy for transient analysis. 33

Nomenclature

$\mathcal{M}$	Second order Constant	
b	Film thickness	m
c_p	Specific heat	$J\,kg^{-1}K^{-1}$
g	Gravitational acceleration	$m\,s^{-2}$
h	Convection coefficient	$W\,m^{-2}K^{-1}$
h_{fg}	Latent heat of vaporization	$J\,m^{-3}$
I	Radiation intensity	$W\,m^{-2}sr^{-1}$
I_b	Blackbody Radiation intensity	$W\,m^{-2}sr^{-1}$
k	Thermal conductivity	$Wm^{-1}K^{-1}$
L	Width	m
p_h	Heating potential	$^{\circ}C$
q''_a	Absorbed heat flux	$W\,m^{-2}$
q'''_g	Internal heat generation	$W\,m^{-3}$
q''_i	Incident heat flux	$W\,m^{-2}$
q''_o	Rejected heat flux	$W\,m^{-2}$
q''_z	Heat flux in the z axis	$W\,m^{-2}$

R_t''	Thermal Resistance	$W^{-1}m^2K$
T	Temperature	$^\circ C$
t	time	s
x	x-directional coordinate	m
y	y-directional coordinate	m
z	z-directional coordinate	m
$\dot{V}$	Volumetric overhead water application rate	$m^3\,s^{-1}$

Dimensionless numbers

$\zeta = z/\delta$ Normalized distance

$\mathrm{Bi} = h\delta/k$ Biot number

$\mathrm{Fo} = \alpha t/\delta^2$ Fourier number

Greek symbols

α	Thermal diffusivity	$m^2\,s^{-1}$
δ	Thickness	m
ν	Kinematic Viscosity	$m^2\,s^{-1}$
Ω	First order Constant	
ω	Solid angle	sr
Ψ	Scattering phase function	
ρ	Density	$kg\,m^{-3}$
$\theta = T - T_\infty$	Temperature difference	$^\circ C$

Subscripts

∞	Ambient
Al	Aluminium
b	Back side
c	Convective
f	Front side
fg	Fibreglass
flame	Flame
g	Hot air
p	Panel
r	Radiative
w	Water

Siglas

ADAI	Association for the Development of Industrial Aerodynamics
WF	Wild fires

Chapter 1

Introduction

Wild fires (WF) are a major problem in Portugal. According to Hernández (2019), "Portugal is by far the Mediterranean country that has suffered the most due to forest fires: in the last 30 years, it has faced more fire incidents with more hectares burned."

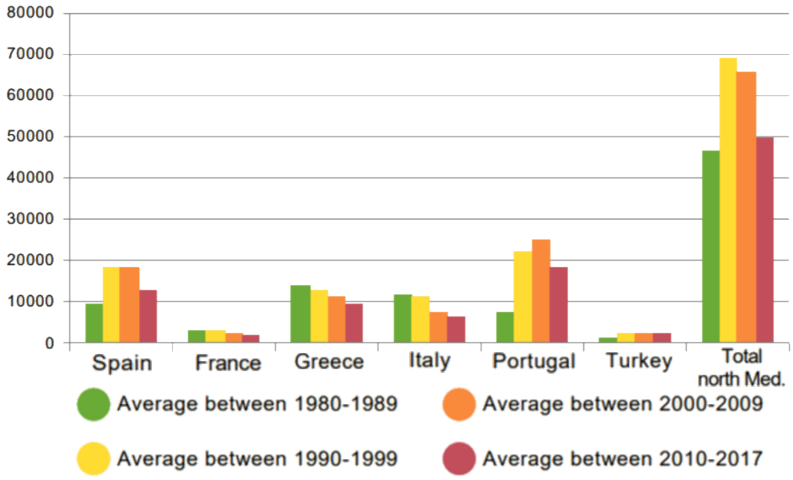

Source: Forest Fires. Sparking firesmart policies in the EU. European Commission, 2018 and official data published by the Directorate of Forestry in Turkey.

Figure 1.1: Number of fires, per decade and country

Analysing data collected by Hernández (2019), Fig. 1.1 shows that the number of fire occurrences in Portugal have been decreasing in the last decade, as well as in most Mediterranean countries. Hernández (2019) explains that it is due to the reduction of people in forests and greater fire crime prosecution in the Mediterranean region.

However, contrarily to almost all Mediterranean countries, Portugal's burnt area has been growing for the last four decades (see Fig. 1.2).

With the increasing wildfire threat, it is imperative to develop new technologies to

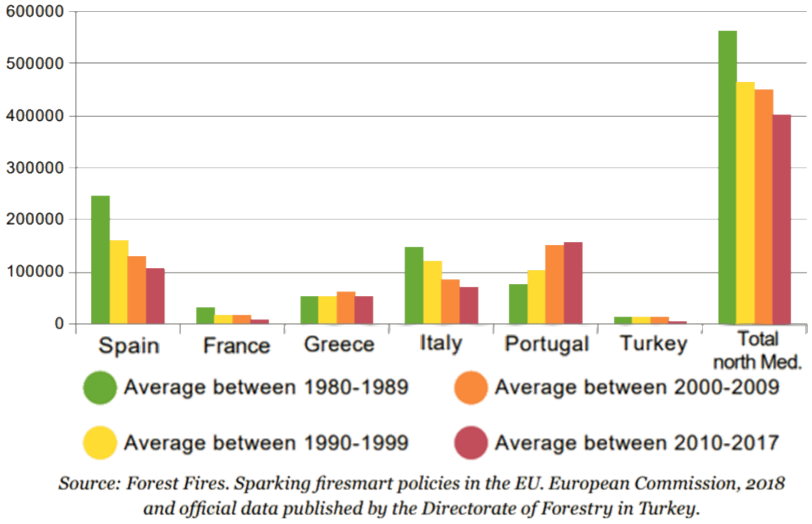

Source: Forest Fires. Sparking firesmart policies in the EU. European Commission, 2018 and official data published by the Directorate of Forestry in Turkey.

Figure 1.2: Burnt area (ha), per decade and country.

better protect people and structures.

1.1. Literature Review

In the available literature, one finds several heat transfer models that analyze the thermal response of fire protection devices to a thermal radiation source, specifically fire-proof barriers. Assuming a general thermal barrier described in Fig. 1.3 with the general heat diffusion equation in Eq. (1.1).

$$\rho_p c_{p,p} \frac{\partial T_p}{\partial t} = \frac{\partial}{\partial x}\left(k_p \frac{\partial T_p}{\partial x}\right) + \frac{\partial}{\partial y}\left(k_p \frac{\partial T_p}{\partial y}\right) + \frac{\partial}{\partial z}\left(k_p \frac{\partial T_p}{\partial z}\right) + q_g''' \tag{1.1}$$

Meredith *et al.* (2013) developed a sprinkler-based fire suppression model with water interacting with a surface. The authors use OpenFOAM to implement the film transport equations and couple them with FireFOAM, validating their numerical approach with experimental results.

The experimental setup shown in Fig. 1.4 consisted of a target panel, an external radiation source, a water spraying system, a collection pan and measuring equipment. The target panel consisted of a $1.9mm$ stainless steel plate coated on both sides painted with a high emissivity material. The heat fluxes used were in the 5 to 33 kW/m^2 range, and water flow rate values per unit length were between 2 and $52g/m/s$ (0.12 to $3.12kg/m/min$). The heat transfer model of the target plate departed from an energy

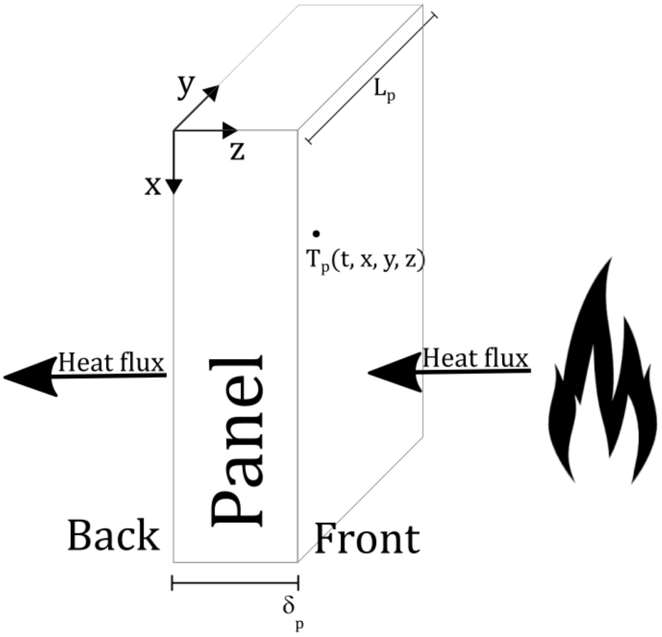
y
z
x
L_p
$T_p(t, x, y, z)$
Heat flux
Heat flux
Panel
Back
Front
δ_p

Figure 1.3: General barrier description

.

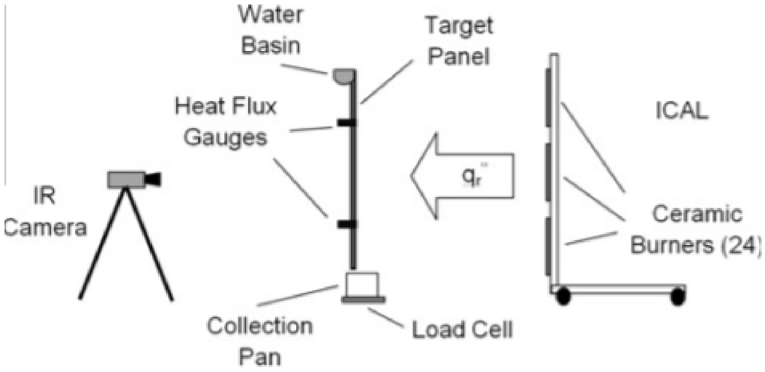
Water Basin
Target Panel
Heat Flux Gauges
ICAL
q_r''
IR Camera
Ceramic Burners (24)
Collection Pan
Load Cell

Figure 1.4: Experimental setup used by Meredith *et al.* (2013)

.

balance to plate as.

$$\delta_p \rho_p c_{p,p} \frac{\partial T_p}{\partial t} = \delta_p \frac{\partial}{\partial x}\left(k_p \frac{\partial T_p}{\partial x}\right) + \delta_p \frac{\partial}{\partial y}\left(k_p \frac{\partial T_p}{\partial y}\right) + q_z''(z=0) - q_z''(z=\delta_p) \qquad (1.2)$$

where $\delta_p, \rho_p, c_{p,p}, k_p$ are the thickness, density, specific heat and thermal conductivity of the panel (p), T is the plate temperature and q_z'' $[W/m^2]$ represents the heat flux in the z axis.

The energy equation in the case of Meredith *et al.* (2013) assumes a uniform temperature distribution on the plate's thickness with no internal heat generation. In fact, Eq. (1.2) is a simplified version of Eq. (1.1) with known heat fluxes in the z axis. Although this local lumped capacitance model is a good approximation of a thin plate with high thermal diffusivity, this is not the case for a barrier made of fibreglass. Previous experiments by Batista (2018) showed that the temperature difference between the front and back side of the fibreglass barrier is significant.

Lev & Strachan (1989) did an experimental study of the water flow rate required to protect metal surfaces exposed to thermal radiation. The experimental work was also supported by a theoretical model.

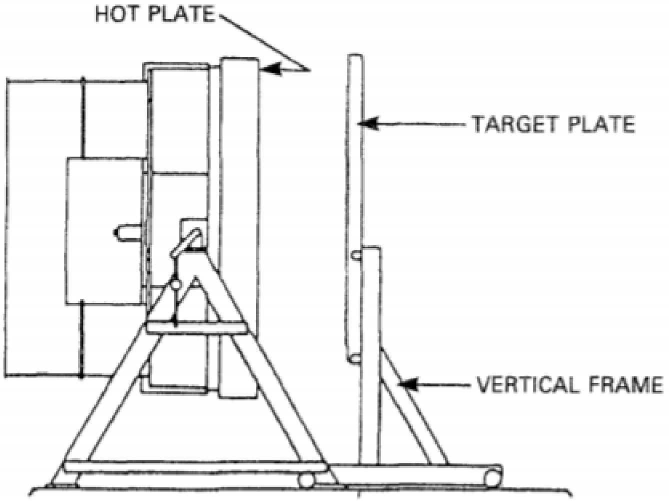

Figure 1.5: Experimental setup used by Lev & Strachan (1989)

The experimental setup consisted of a target plate, external radiation source, water spraying devices and measuring equipment, as shown in Fig. 1.5. The target panel is made of 10 mm thick steel. Heat fluxes employed were up to $70 kW/m^2$ range, water flow values in 6.4 to $21.2 kg/m/min$ (for film cooling).

For film cooling, the following model was used. It was assumed that all the input heat was removed by the water film (steady-state), raising its temperature.

$$\Delta T_w(x) = \frac{q''_{i,r}\ L_p\ x}{\dot{V} \rho_w\ c_{p,w}} \tag{1.3}$$

with $q''_{i,r}$ as the incident radiation $[W/m^2]$, L_p as the plate width $[m]$, x as the distance below top of the plate $[m]$, $\dot{V}$ as the volumetric overhead water application rate $[m^3/s]$, ρ_w as the water density $[kg/m^3]$ and $c_{p,w}$ as the specific heat of water $[J/kg\ K]$.

When boiling occurs, the water vaporization rate is

$$\Delta \dot{V}(x) = \frac{q''_{i,r} L_p x - \dot{V} \rho_w c_{p,w} (100 - T_{0,w})}{h_{fg}} \tag{1.4}$$

with $T_{0,w}$ as the initial water temperature $[K]$ and h_{fg} as the latent heat of vaporization for water $[J/m^3]$.

With Eq. (1.4) and (1.5), the water temperature and water flow rate at a given height of the plate are calculated. Then, the film thickness is calculated with the following equation

$$b(x) = \left(\frac{2.4 \dot{V} \nu_w}{L_p g} \right)^{1/3} \tag{1.5}$$

with ν_w as the water kinematic viscosity $[m^2/s]$ and g as the gravitational acceleration $[m/s^2]$.

Using Beer's Law, the flux absorbed by the water film is calculated. Assuming the remaining heat is taken up by the plate, it is then removed by the water under steady-state conditions, satisfying the following equation

$$T_p(x) = T_w(x) + \frac{q''_z(z = \delta_p)}{h} \tag{1.6}$$

with $T_p(x)$ as the plate temperature $[K]$, $T_w(x)$ as the water film temperature $[K]$, q_z" as the heat flux from plate $[W/m^2]$ and h as the heat transfer coefficient $[W/m^2 K]$.

This theoretical model only considers the steady-state water flow required. The model also assumes that the back-side of the plate is insulated and, therefore, all the heat is removed by the water. Both aspects make this model inadequate for a real fire front scenario, where the heat fluxes are transient.

Hsu *et al.* (2011) developed a one-dimensional numerical model for thin fire blanket materials, considering both conductive and radiative heat transfer. Bench scale experiments were conducted to compare with the theoretical results. No water cooling was tested.

The experimental setup consisted of the test fabric, heat source and measuring equipment. Two types of heat sources were used: a propane fuelled Meker burner or a radiant cone.

The configuration of the model is in Fig. 1.7.

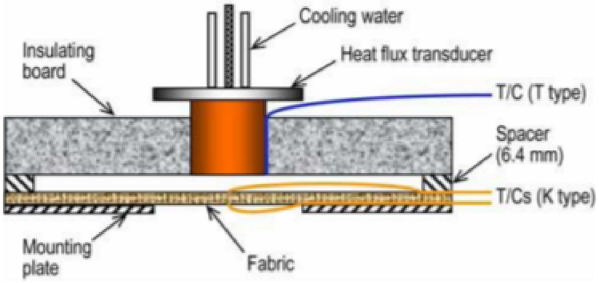
Cooling water
Insulating board
Heat flux transducer
T/C (T type)
Spacer (6.4 mm)
T/Cs (K type)
Mounting plate
Fabric

Figure 1.6: Experimental setup used by Hsu *et al.* (2011).

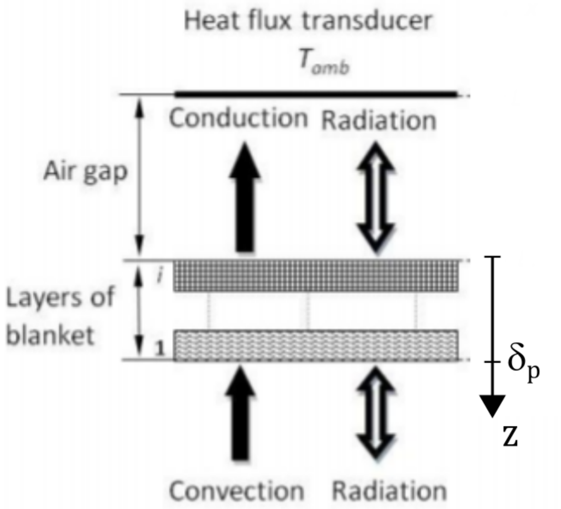
Heat flux transducer
T_{amb}
Conduction
Radiation
Air gap
Layers of blanket
i
1
δ_p
z
Convection
Radiation

Figure 1.7: Fire blanket model by Hsu *et al.* (2011).

The governing equation used in the model is the uni-dimensional version of Eq. (1.1) expressed as:

$$C^A(T_p)\frac{\partial T_p}{\partial t} = \frac{\partial}{\partial z}(k_p(T_p)\frac{\partial T_p}{\partial z}) - \frac{\partial q''_{z,r}}{\partial z} \tag{1.7}$$

where C^A is the apparent heat capacity of the panel containing the energy generated by chemical reactions in the fabric per unit volume, and $q''_{z,r}$ is the radiative heat flux absorbed by the blanket in the z axis, considering $\partial q_{z,r}/\partial z < 0$, as an internal heat generation term.

The radiative heat flux is given by:

$$q_r(z) = \int_{4\pi} I(z, \hat{s})\hat{s}d\omega \tag{1.8}$$

with I as the radiation intensity, $\hat{s}$ as the unit vector and ω as the radiation solid angle [sr]. The radiation intensity is obtained by the radiation transfer equation:

$$\frac{dI}{ds} = \kappa I_b(s) - \beta I(s) + \frac{\sigma_s}{4\pi}\int_{4\pi} I(\hat{s}_i)\Psi(\hat{s}_i, \hat{s})d\omega_i \tag{1.9}$$

with s as the coordinate along the path of radiation, I_b as the blackbody radiation intensity, κ as the absorption coefficient,σ_s as the scattering coefficient, $\beta = \kappa + \sigma_s$ as the attenuation coefficient and Ψ as the scattering phase function. This equation translates the increase in radiation intensity in the medium due to emissivity and "in-scattering" and the decrease in intensity due to absorptivity and "out-scattering".

The initial condition for the entire domain is the ambient temperature. The boundary condition at the front surface for radiative heating is:

$$q''_{z,r}(z = \delta_p) = -q''_{i,r} \tag{1.10}$$

while for convective heating is

$$k_p \left.\frac{\partial T_p}{\partial z}\right|_{z=\delta_p} = h_{front}(T_{flame} - T_p(z = \delta_p)) \tag{1.11}$$

At the back surface, the radiative flux boundary condition is

$$q''_{z,r}(z = 0) = \sigma T^4_{amb} \tag{1.12}$$

This model is very comprehensive, describing both conductive and radiative heat transfer phenomena in the panel material. However, it is a very complex model which requires a numerical implementation. Also, the back side boundary condition lacks convection which occurs in a vertical panel in real case scenario.

In conclusion, there are already available in the literature multiple models with various approaches to a fire-proof barrier problem. For this study, none of the models would allow to generate an analytical solution for predicting the temperature distribution of the thermal barrier, and its evolution under a transient heat flux exposure.

1.2. Objectives

The Fireprotect project seeks to develop new solutions for protection of people and infrastructures against WF. One of the mechanisms conceived by this project is a water-cooled fireproof barrier, which is the subject of this work. This barrier, made from fibreglass (and an aluminium coating), resists to high temperatures and radiation intensities. And the purpose of this barrier is to stop the progression of a fire front. However, its optimization implies developing a theoretical model able to describe its thermal response to a transient heat flux. Therefore, the objectives of this thesis are:

- the formulation of a heat transfer model describing the fireproof thermal barrier
- the implementation of an approximation strategy for the analytical solution for the inverse Laplace transformation
- the testing the model in simple heat flux boundary conditions to assess its limitations
- and, finally, the experimental validation of the semi-analytical model derived.

Chapter 2

Coated thermal barrier heat transfer model

The modeled thermal system is illustrated in Fig. 2.1 where the front side of the fiberglass of thickness δ_{fg} has an aluminum layer of thickness δ_{Al} facing the flame front. The absorbed heat flux in the front side can be convective and/or radiative and is represented by $q''_{a,(r+c)}$ while the heat flux out the back side is convective and represented by $q''_{o,c}$.

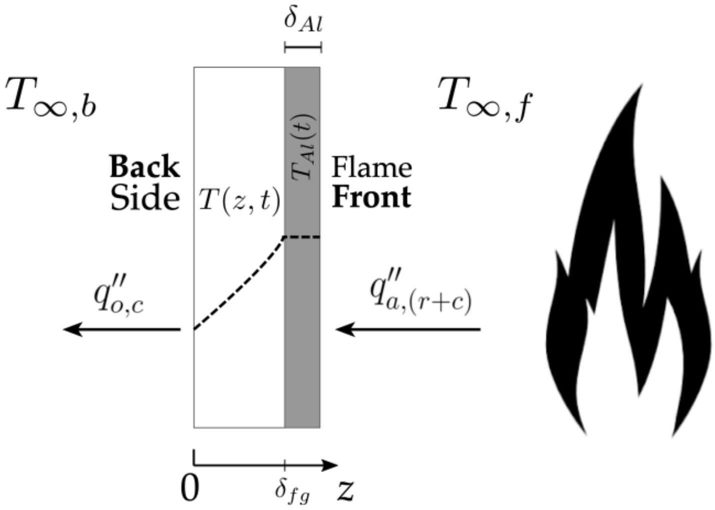
δ_{Al}
$T_{\infty,b}$
$T_{\infty,f}$
$T_{Al}(t)$
Back Side
$T(z,t)$
Flame Front
$q''_{o,c}$
$q''_{a,(r+c)}$
0
δ_{fg}
z

Figure 2.1: Schematic of the fiberglass coated with aluminum.

Any variations of the fiberglass temperature in the heat transfer area (x, y) facing the flame produce negligible changes in the x and y directions relative to the variations induced in its thickness (z). Therefore, the modeling of the heat transfer inside the fiberglass portion of a fire thermal barrier ($T_p(z) = T_{fg}(z)$) considers a 1-D energy balance. To further simplify the model:

- Only conductive heat transfer was considered in the fibreglass region. It is assumed that all the incident radiative flux is either absorbed or reflected by the aluminium coating.

- No internal heat generation was considered, as it was assumed that no radiation was being transfered into the medium and no chemical reactions were taking place.

With all these simplifications, the general heat conduction equation in Eq. (1.1) becomes Eq. (2.1):

$$\frac{\partial T_{fg}(z,t)}{\partial t} = \alpha_{fg} \frac{\partial^2 T_{fg}(z,t)}{\partial z^2} \tag{2.1}$$

where α $[m^2/s]$ is the thermal diffusivity of the fibreglass. Initially, one assumes that the barrier is at ambient temperature. On the back side of the fiberglass, one considers that heat transfer occurs by convection (boundary condition at $z = 0$). No radiative heat transfer was considered due to the lower temperature usually measured in the back side. On the front side, the contact with the aluminium layer sets the second boundary condition at $z = \delta_{fg}$.

$$\text{Initial condition:} \qquad T_{fg}(z,0) = T_\infty \tag{2.2}$$

$$\text{Boundary condition at } z = 0: \qquad k_{fg} \left. \frac{\partial T_{fg}(z,t)}{\partial z} \right|_{z=0} = h_b(T_{fg}(0,t) - T_\infty) \tag{2.3}$$

$$\text{Boundary condition at } z = \delta_{fg}: \qquad T_{fg}(\delta_{fg},t) = T_{Al}(t) \tag{2.4}$$

The aluminium layer has a very high thermal diffusivity and reduced thickness, so it is assumed that its thermal resistance is negligible, leading to a time evolution of its temperature with a uniform spacial distribution,

$$T_p(\delta_{fg} \leq z \leq \delta_{fg} + \delta_{Al}, t) = T_{Al}(t)$$

Therefore, to relate the total heat flux from the flame radiation and forced convection from the heated air, one applies the conservation of energy to the aluminium layer as

$$\delta_{Al} c_{Al} \rho_{Al} \frac{\partial T_{Al}}{\partial t} = q''_{a,(r+c)}(t) - k_{fg} \left. \frac{\partial T_{fg}(z,t)}{\partial z} \right|_{z=\delta_{fg}} \tag{2.5}$$

Substituting Eq. (2.4) in Eq. (2.5) and rearranging the terms, the boundary condition at $z = \delta_{fg}$ becomes

$$k_{fg} \left. \frac{\partial T_{fg}(z,t)}{\partial z} \right|_{z=\delta_{fg}} = q''_{a,(r+c)}(t) - \delta_{Al} c_{Al} \rho_{Al} \left. \frac{\partial T_{fg}(z,t)}{\partial t} \right|_{z=\delta_{fg}} \tag{2.6}$$

For the elaboration of an approximate solution for the formulations above, one normalizes the parameters involved considering the fiberglass thickness (δ_{fg}) as the length scale, the penetration time of a perturbation through the fiberglass thickness ($\tau = \delta_{fg}^2/\alpha$) as the timescale, and the temperature difference of any point z relative to the environment (T_∞). Applying these variable changes, Eq. (2.1), (2.2), (2.3) and (2.6) become Eq. (2.7), (2.8), (2.9) and (2.10), respectively.

$$\frac{\partial^2 \theta_{fg}(\zeta, \mathrm{Fo})}{\partial \zeta^2} = \frac{\partial \theta_{fg}(\zeta, \mathrm{Fo})}{\partial \mathrm{Fo}} \tag{2.7}$$

$$\theta_{fg}(\zeta, 0) = 0 \tag{2.8}$$

$$\left. \frac{\partial \theta_{fg}(\zeta, \mathrm{Fo})}{\partial \zeta} \right|_{\zeta=0} = \mathrm{Bi}\ \theta_{fg}(0, \mathrm{Fo}) \tag{2.9}$$

$$\left. \frac{\partial \theta_{fg}(\zeta, \mathrm{Fo})}{\partial \zeta} \right|_{\zeta=1} = \phi_h(\mathrm{Fo}) - C^*_{t,f} \left. \frac{\partial \theta_{fg}(\zeta, \mathrm{Fo})}{\partial \mathrm{Fo}} \right|_{\zeta=1} \tag{2.10}$$

with $\zeta = z/\delta_{fg}$ as the dimensionless length, Fo$= \frac{t\alpha}{\delta_{fg}^2}$ is the Fourier number, Bi $= h_{back}\delta_{fg}/k_{fg}$ as the Biot number, $\theta_{fg}(\zeta, \mathrm{Fo}) = T_{fg}(\zeta, \mathrm{Fo}) - T_\infty$ as the temperature difference, $\phi_h(\mathrm{Fo}) = \frac{\delta_{fg}}{k_{fg}} q''_{a,(r+c)}(\mathrm{Fo})$ as the heating potential since it is the product of the fiberglass thermal resistance by the heat flux at the flame front side, and $C^*_{t,f} = \frac{\delta_{Al} c_{Al} \rho_{Al}}{\delta_{fg} c_{fg} \rho_{fg}}$ as the ratio associated with the thermal capacity of the aluminium layer relative to the fiberglass.

Using Laplace Transforms to the temperature difference term,

$$\mathcal{L}\{\theta_{fg}(\zeta, \mathrm{Fo})\} = \Theta(\zeta, s) \tag{2.11}$$

one can transform the partial differential equation Eq. (2.7) in:

$$s\Theta(\zeta,s)-\theta_{fg}(\zeta,0)=s\Theta(\zeta,s)=\frac{\partial^2\Theta(\zeta,s)}{\partial\zeta^2} \tag{2.12}$$

and boundary conditions in:

$$\frac{\partial\Theta(0,s)}{\partial\zeta}=\mathrm{Bi}\ \Theta(0,s) \tag{2.13}$$

$$\frac{\partial\Theta(1,s)}{\partial\zeta}=\Phi_h(s)-C^*_{t,f}\ s\ \Theta(1,s) \tag{2.14}$$

The ODE in Eq. (2.12) can be solved with Wolfram Mathematica using the boundary conditions of Eq. (2.13) and (2.14), resulting in:

$$\Theta(\zeta,s)=F(\zeta,s)\times\Phi_h(s) \tag{2.15}$$

Analysing Eq. (2.15), one can interpret $\Theta(\zeta,s)$ as the system response to the heat flux perturbation from the flame, Φ_h as the input and $F(\zeta,s)$ as a transfer function, similar to control systems. Therefore, the accuracy of the solution depends on the approximation applied to the transfer function $F(\zeta,s)$ defined as

$$F(\zeta,s)=\frac{\sqrt{s}Cosh(\sqrt{s})+\mathrm{Bi}Sinh(\sqrt{s}\zeta)}{\sqrt{s}(\mathrm{Bi}+C^*_{t,f}s)Cosh(\sqrt{s})+(1+C^*_{t,f}\mathrm{Bi})sSinh(\sqrt{s})} \tag{2.16}$$

The Inverse Laplace Transform will be the final solution

$$\theta_{fg}(\zeta,\mathrm{Fo})=\mathcal{L}^{-1}\{F(\zeta,s)\times\Phi_h(s)\}=\int_0^{\mathrm{Fo}}f(\zeta,\mathrm{Fo}-\tau)\times\phi_h(\tau)d\tau \tag{2.17}$$

Using the Laplace Transform properties, the temperature potential $\phi_h(\mathrm{Fo})$ can be an arbitrary function proportional to the heat flux. But, to determine the function $f(\zeta,\mathrm{Fo})=\mathcal{L}^{-1}\{F(\zeta,s)\}$, due to its complexity, it is necessary to simplify $F(\zeta,s)$ before its return to the Fourier domain. The error of a certain approximation will vary throughout the Laplace domain of the transfer function and changes the system's response in ways that are not well documented.

To find an approximation, the approach followed begins by analyzing a time interval, small enough to consider the system in a quasi steady-state (qss), similarly to taking a picture of the temperature distribution with a certain exposure time. In such quasi steady-state condition, the temperature distribution inside the thermal barrier follows the relation $\frac{\partial^2\theta_{fg}(\zeta,\mathrm{Fo})}{\partial\zeta^2} \approx 0$, which results in the following transfer function in the Laplace domain

$$F_{qss}(\zeta) = \frac{1}{\mathrm{Bi}} + \zeta \tag{2.18}$$

By definition, this transfer function describes a system's response at quasi steady-state, and to understand what is the relationship between this transfer function and the exact transfer function, Fig. 2.2 allows their visualization in the Laplace Domain. The variable s is a complex number, thus, plotting the absolute value of the function in the remaining axis. For this analysis, only the complex plane with positive real part is shown.

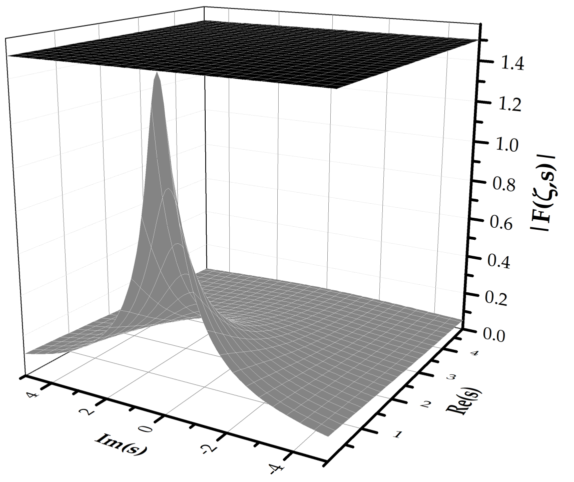

Figure 2.2: Exact transfer function (gray) and steady-state transfer function (black) (For $\mathrm{Bi} = 1$, $C^*_{t,f} = 0.5$ and $\zeta = 0.5$).

Fig. 2.2 shows that the transfer functions only intersect at the origin of the complex plane. From this information, one can formulate the hypothesis that an accurate representation of the system response for higher Fourier numbers implies the approximation of the exact transfer function to another around the origin of the complex plane (see Appendix A).

Therefore, using Wolfram Mathematica to obtain a Padé Approximant around $s \to 0$ with a zeroth order polynomial in the numerator and a first order polynomial in the denominator (as in a first order system), the approximant results in

$$F(\zeta, s) \approx \frac{\frac{1}{\mathrm{Bi}} + \zeta}{1 + \Omega(\zeta)s} \tag{2.19}$$

with

$$\Omega(\zeta) = \frac{6 + 6\ C^*_{t,f}(1 + \mathrm{Bi})(1 + \mathrm{Bi}\zeta) + \mathrm{Bi}(3 + \zeta(6 - 3\zeta - \mathrm{Bi}(\zeta^2 - 3)))}{6\mathrm{Bi}(1 + \mathrm{Bi}\zeta)} \tag{2.20}$$

The function $\Omega(\zeta)$ is the equivalent to the time constant of a first order system for each plane located at ζ in the material, although, in this case, being defined in the Fourier domain, $\Omega(\zeta)$ is dimensionless. In Eq. (2.19), the numerator represents the quasi steady-state transfer function. It is also noteworthy that an order larger than one in the denominator would lead to instabilities in the approximant solution in some regions.

Fig. 2.3 compares the exact solution (2.16) with the approximated transfer function in (2.19), including also the quasi-steady-state result.

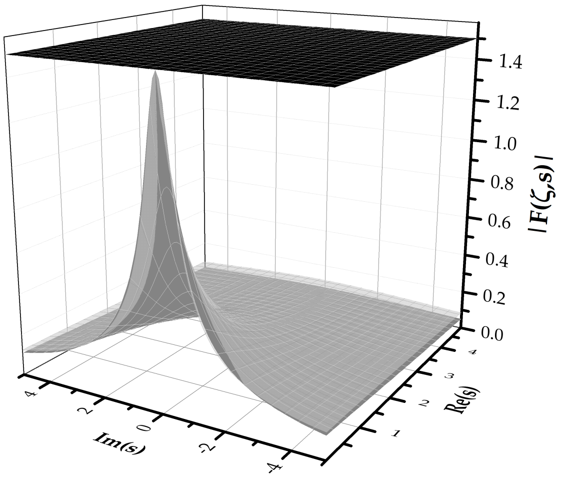

Figure 2.3: Exact transfer function (dark grey), Approximate function (light grey) and Quasi-static function (black) (For $\mathrm{Bi} = 1$, $C^*_{t,f} = 0.5$ and $\zeta = 0.5$).

The figure shows that the approximation for higher s values looses accuracy but doesn't diverge considerably.

The function $f(\zeta, \mathrm{Fo})$ is now given by the Inverse Laplace Transform of the new approximate transfer function $F(\zeta, s)$. The result is in Eq. (2.21).

$$f(\zeta, \mathrm{Fo}) = \left(\frac{1}{\mathrm{Bi}} + \zeta\right) \frac{e^{-\frac{\mathrm{Fo}}{\Omega(\zeta)}}}{\Omega(\zeta)} \tag{2.21}$$

Using Eq. (2.17), the general $\theta_{fg}(\zeta, \mathrm{Fo})$ formula is:

$$\theta_{fg}(\zeta, \mathrm{Fo}) = \int_0^{\mathrm{Fo}} (\frac{1}{\mathrm{Bi}} + \zeta) \frac{e^{-\frac{\mathrm{Fo}-\tau}{\Omega(\zeta)}}}{\Omega(\zeta)} \times \phi_h(\tau) d\tau \tag{2.22}$$

Simplifying the integral:

$$\theta_{fg}(\zeta, \mathrm{Fo}) = (\frac{1}{\mathrm{Bi}} + \zeta) \frac{e^{-\frac{\mathrm{Fo}}{\Omega(\zeta)}}}{\Omega(\zeta)} \int_0^{\mathrm{Fo}} e^{\frac{\tau}{\Omega(\zeta)}} \times \phi_h(\tau) d\tau \tag{2.23}$$

At this point is possible to substitute ϕ_h with simple functions and get the analytical result for $\theta_{fg}(\zeta, \mathrm{Fo})$, given the simplicity of the integrand function.

2.1. Theoretical Testing of the heat transfer model

The evaluation of the error of the approximation previously made in the Laplace domain, recurs to the need for determining a reference solution. Considering the absence of exact analytical solutions for this transient phenomenon, one can numerically solve Eq. (2.7) using finite differences with a dense mesh, choosing different heat flux functions as boundary conditions. The considered meshes are shown in Table 2.1.

Table 2.1: Mesh information.

Mesh	$\Delta\zeta$	$\Delta\mathrm{Fo}$
1	0.2	0.01
2	0.1	0.0025
3	0.0625	0.0005
4	0.05	0.0001

From mesh 1 to 4 the ζ resolution was increased. To guarantee the stability of the solution, the Fo resolution had to be increased as well. Each mesh solution is compared to the solution generated by mesh 4 in Fig. 2.4.

This figure shows that the average error of mesh 2 and 3 is less than 1%. It is then reasonable to conclude that the solution doesn't change appreciably for resolutions

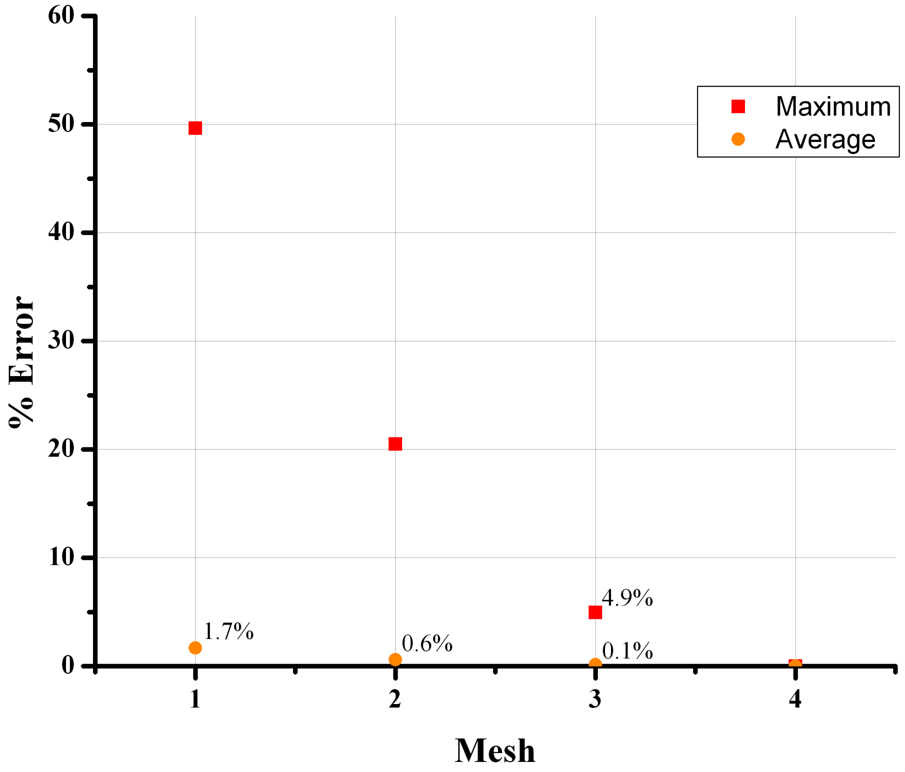

Figure 2.4: Average error and maximum error percentage evolution relative to mesh 4 (For Bi $= 1$, $C^{*}_{t,f} = 0.5$ and $\phi_h = 100°C$).

above those used in mesh 2. For this testing, mesh 3 was used because its maximum error percentage is below 5% relative to mesh 4.

The first test considers a constant heat flux, and the results are depicted in Fig. 2.5.

From Fig. 2.5, it is clear that the steady state is accurately represented, as expected. However, for small Fourier (Fo) values, the approximate solution is less accurate, especially for $\zeta = 0$.

The second test considers the solution for a parabolic function applied in ϕ_h. At Fo=0, $\phi_h = 0$, then at a certain Fourier number Fo_{max}, ϕ_h reaches its maximum, and decreases afterward until it reaches $\phi_h = 0$ at Fo $= 2\text{Fo}_{max}$. Figures 2.6 and 2.7 compare the result obtained with the reference numerical solution.

From the results depicted, one concludes that the approximation is accurate for transient heat flux conditions, although mildly underestimating the system response time. It is noteworthy that the error of the model solution is higher for faster changes

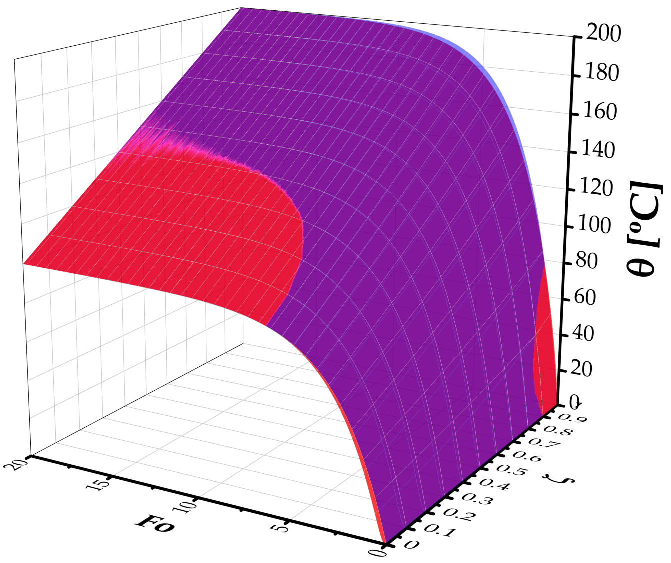

Figure 2.5: Approximate solution (blue) and reference solution (red) (For Bi $= 1$, $C^*_{t,f} = 0.5$ and $\phi_h = 100°C$).

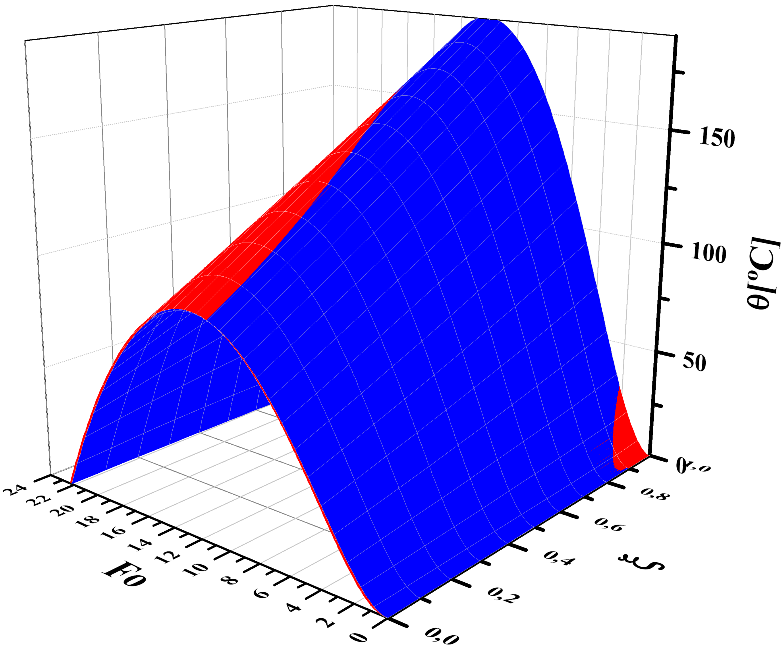

Figure 2.6: Approximate solution (blue) and reference solution (red) (For $\mathrm{Fo}_{max} = 10$, $\mathrm{Bi} = 1$ and $C^*_{t,f} = 0.5$).

in the heat fluxes.

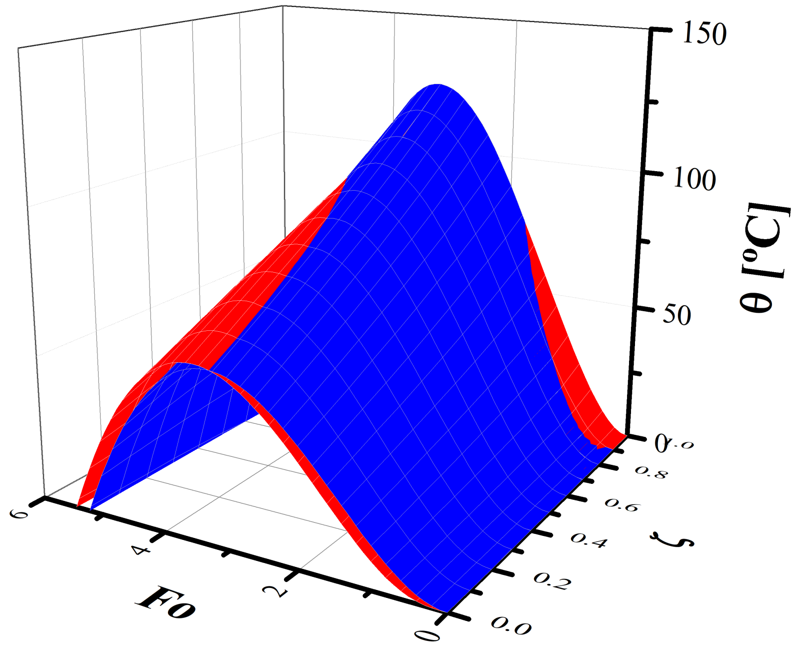

Figure 2.7: Approximate solution (blue) and reference solution (red) (For $\text{Fo}_{max} = 2$, $\text{Bi} = 1$ and $C^*_{t,f} = 0.5$).

2.2. Improved approximation for the barrier's backside thermal behaviour

In cases in need of a more accurate solution for the back side of the barrier in step functions, a second order approximation in the transfer function may be used:

$$F(\zeta, s) \approx \frac{\frac{1}{\text{Bi}} + \zeta}{1 + \Omega(\zeta)s + \mathcal{M}(\zeta)s^2} \tag{2.24}$$

For $\zeta = 0$, the constants become:

$$\Omega(0) = \frac{1}{2} + C^*_{t,f} + \frac{1 + C^*_{t,f}}{\text{Bi}} \tag{2.25}$$

$$\mathcal{M}(0) = \frac{4 + \text{Bi} + 4C^*_{t,f}(3 + \text{Bi})}{24\ \text{Bi}} \tag{2.26}$$

With these constants, for all positive values of Bi and $C^*_{t,f}$, the transfer function stability criterion is satisfied. The inverse Laplace Transform of this new transfer function is:

$$f(0,\mathrm{Fo}) = \left(\frac{1}{\mathrm{Bi}} + 0\right) \frac{1}{\sqrt{\Omega(0)^2 - 4\mathcal{M}(0)}} \left[e^{\mathrm{Fo}(A+B)} - e^{\mathrm{Fo}(A-B)}\right] \tag{2.27}$$

where $A = \frac{-\Omega(0)}{2\mathcal{M}(0)}$ and $B = \frac{\sqrt{\Omega(0)^2 - 4\mathcal{M}(0)}}{2\mathcal{M}(0)}$.

The new solution for the back side of the barrier is:

$$\begin{aligned}\theta_{fg}(0,\mathrm{Fo}) = \left(\frac{1}{\mathrm{Bi}} + 0\right) \frac{1}{\sqrt{\Omega(0)^2 - 4\mathcal{M}(0)}} \Bigg[& e^{\mathrm{Fo}(A+B)} \int_0^{\mathrm{Fo}} e^{-(A+B)\tau} \times \phi_h(\tau) d\tau \\ & -e^{\mathrm{Fo}(A-B)} \int_0^{\mathrm{Fo}} e^{-(A-B)\tau} \times \phi_h(\tau) d\tau \Bigg]\end{aligned} \tag{2.28}$$

Fig. 2.8 contains the comparison of this second order approximation with the first order approximation and the reference solution for a step function. Results evidence the greater accuracy of the second order approximation for low Fourier (Fo) values, while for higher Fo values, there is no advantage in using a second order approximation.

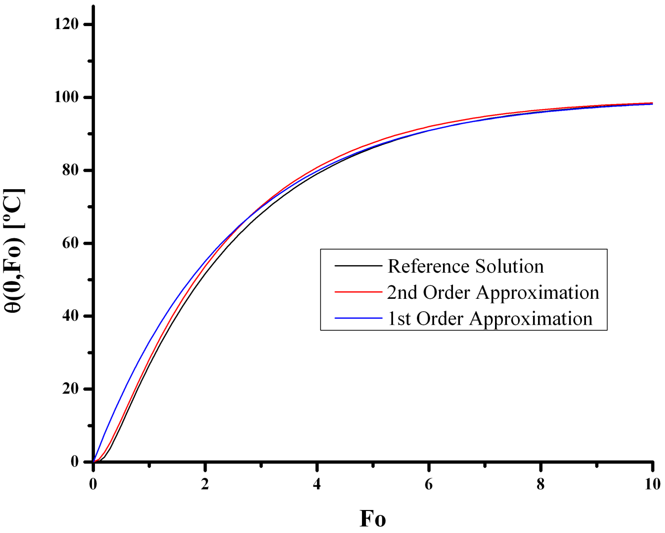

Figure 2.8: 1st order Approximate solution (blue), 2nd order Approximate solution (red) and reference solution (black) (For Bi = 1, $C^*_{t,f} = 0.5$ and $\phi_h = 100°C$).

Chapter 3

Experimental Setup for heat transfer model validation

An experimental setup built to validate the heat transfer model developed in chapter 2 consists of a heat gun that generates a convective heat source impinging onto a sample of the thermal barrier under research, as depicted in Fig. 3.1. The validation of the heat transfer model includes the comparison of measurements and predictions of the temperature in both front and back surfaces when exposed to a heat source. An aluminium structure with a hinge in the back supports the heat gun and allows it to rotate upwards while is reaches a steady-state condition, blowing the hot air away from the test zone. After reaching steady-state, one suddenly lowers the heat gun exposing the test zone to a flow with constant properties.

The measurement of the surface temperature with K-type thermocouples attached to the front and back surfaces, allows capturing the surface thermal behaviour. Additionally, one measures the incident hot air temperature with a K-type thermocouple located near the front surface. This last thermocouple did not have a fast enough response time to measure a sudden change in air temperature. In order to detect more precisely when the hot air started flowing in the test zone, a trigger switch was installed in the base of the structure, which starts acquiring data after confirmation of an attained steady-state condition. A DT9828 board from DataTranslation allows acquiring data of all thermocouples and switch with a sample rate per channel of 150 Hz.

The barrier is made of fibreglass with an aluminium coating. Using a caliper, the

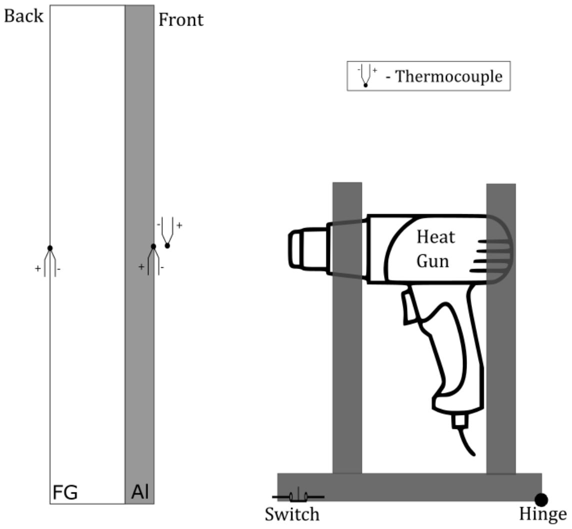
Back
Front
- Thermocouple
Heat Gun
FG
Al
Switch
Hinge

Figure 3.1: Illustration of the experimental setup built to validate the heat transfer model.

thickness of both fibreglass and aluminium were measured (see Table 3.1). All the thermal properties of the aluminium layer were taken from Incropera (2006), and the thermal properties of the fibreglass fabric were taken from Redmond & Mastropietro (2015) and manufacturer's catalogue.

However, for accuracy purposes, the fibreglass' thermal conductivity is determined, experimentally, using a heat flux sensor (Captec sensor with buit-in T-type thermocouple) on the front side, as depicted in Fig. 3.2 (experimental procedure in Appendix B).

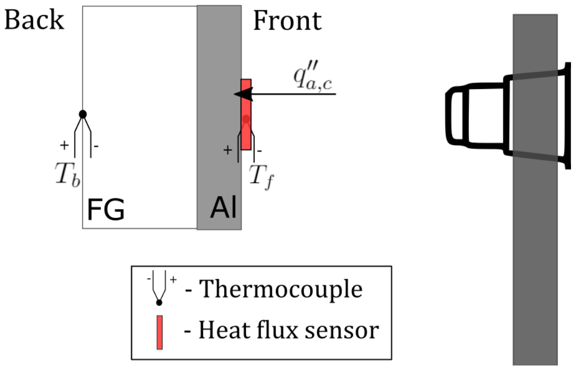
Back
Front
$q''_{a,c}$
T_b
T_f
FG
Al
- Thermocouple
- Heat flux sensor

Figure 3.2: Experimental Setup to determine k_{fg}

After reaching steady-state, the values measured by the heat flux sensor, front and back surface temperatures in multiple time instants were stored. The thermal conductivity was then calculated with the following equation (details in Appendix C):

$$k_{fg} = \frac{q''_{a,c}\,\delta_{fg}}{T_f - T_b} \tag{3.1}$$

All the properties considered are presented in the next table.

Table 3.1: Thermal and geometric properties of the thermal barrier's materials.

Property	δ $[\mu m]$ (exp.)	ρ $[kg/m^3]$	c_p $[J/(kg\cdot K)]$	k $[W/(m\cdot K)]$	$R''_t[(m^2\cdot K)/W]$
fg	300±1.7%	1373	$700-900$	$0.03315 \pm 0.15\%$	9×10^{-3}
Al	40 ±12.5%	2703	903	237	2×10^{-7}

Under these conditions, the absorbed heat flux is convective and given by:

$$q''_{a,(r+c)}(t) = q''_{a,c}(t) = h_f(t)\ (T_g(t) - T_f(t)) \tag{3.2}$$

where T_g is the hot air temperature and $h_f(t)$ is the convection coefficient in the front side of the barrier. To determine both $h_f(t)$ and h_b, one uses the steady-state (ss) temperature data, considering the following relations:

$$\left(q''_{a,c}\right)_{ss} = k_{fg}\frac{(T_f)_{ss} - (T_b)_{ss}}{\delta_{fg}} \tag{3.3}$$

$$\left(q''_{a,c}\right)_{ss} = h_{f,ss}\ ((T_g)_{ss} - (T_f)_{ss}) \tag{3.4}$$

$$\left(q''_{a,c}\right)_{ss} = h_b\ ((T_b)_{ss} - T_\infty) \tag{3.5}$$

The steady state heat flux, calculated using Eq. (3.3), allows to calculate $h_{f,ss}$ and h_b from Eq. (3.4) and (3.5), respectively. Afterward, the heating potential follows the relation:

$$\phi_h(\mathrm{Fo}) = \frac{\delta_{fg}}{k_{fg}} h_f(\mathrm{Fo})(\theta_g(\mathrm{Fo}) - \theta_{fg}(1,\mathrm{Fo})) \tag{3.6}$$

where $\theta_g(\mathrm{Fo}) = T_g(\mathrm{Fo}) - T_\infty$.

3.1. Model changes to account for experimental conditions

The thermocouples on both sides of the barrier attached with aluminium foil tape, imply an additional thickness in the model. Although the tape's thickness is only

$40\mu m$, it is enough to skew the results in a barrier with $0.34mm$ thickness. However, the model doesn't include the possibility for an aluminium layer in the back side. Therefore, this leads to a generalization of the back side boundary condition as

$$\left.\frac{\partial\theta_{fg}(\zeta,\mathrm{Fo})}{\partial\zeta}\right|_{\zeta=0} = \mathrm{Bi}\ \theta_{fg}(0,\mathrm{Fo}) + C^*_{t,b}\left.\frac{\partial\theta_{fg}(\zeta,\mathrm{Fo})}{\partial\mathrm{Fo}}\right|_{\zeta=0} \tag{3.7}$$

where

$$C^*_{t,b} = \frac{\delta_b\ c_{p,b}\ \rho_b}{\delta_{fg}c_{p,fg}\rho_{fg}} \tag{3.8}$$

with δ_b, $c_{p,b}$ and ρ_b being the tape's thickness, specific heat and density, respectively. Using the same method shown in the last chapter, table 3.2 synthesizes the new constants $\Omega(\zeta)$ and $\mathcal{M}(\zeta)$ obtained in the barrier's boundaries ($\zeta \in \{0,1\}$).

Table 3.2: New constants of the modified model to include the aluminium tape used to attach thermocouples in the experimental setup.

	$\zeta = 0$	$\zeta = 1$
$\Omega(\zeta)$	$\frac{2+\mathrm{Bi}+2\ C^*_{t,f}\ (1+\mathrm{Bi})+2\ C^*_{t,b}}{2\ \mathrm{Bi}}$	$\frac{\mathrm{Bi}^2+3\ C^*_{t,f}\ (1+\mathrm{Bi})^2+3\ (1+\mathrm{Bi}+C^*_{t,b})}{3\ \mathrm{Bi}\ (1+\mathrm{Bi})}$
$\mathcal{M}(\zeta)$	$\frac{4+\mathrm{Bi}+12\ C^*_{t,b}+4\ C^*_{t,f}\ (3+\mathrm{Bi}+6\ C_{tb})}{24\ \mathrm{Bi}}$	< 0 (unstable solution)

3.2. Application of the model modified for the experimental setup

Placing the heating potential from Eq. (3.6) in the simplified model in Eq. (2.23), one obtains:

$$\theta_{fg}(\zeta,\mathrm{Fo}) = \left(\frac{1}{\mathrm{Bi}}+\zeta\right)\frac{e^{-\frac{\mathrm{Fo}}{\Omega(\zeta)}}}{\Omega(\zeta)}\int_0^{\mathrm{Fo}} e^{\frac{\tau}{\Omega(\zeta)}} \times \frac{\delta_{fg}}{k_{fg}}h_f(\tau)(\theta_g(\tau)-\theta_{fg}(1,\tau))d\tau \tag{3.9}$$

Eq. (3.9) shows the solution $\theta_{fg}(\zeta,\mathrm{Fo})$ is not explicit. The reason lies in the absorbed convective flux that depends on the front surface temperature (it also occurs for a radiative heat source). To solve this, first, one solves Eq. (3.9) for $\zeta = 1$. Applying a numerical integration, for example, using the trapezoidal rule:

$$
\begin{aligned}
&\boldsymbol{\theta_{fg}(1,\mathrm{Fo}_n)} = \left(\frac{1}{\mathrm{Bi}}+1\right)\frac{e^{-\frac{\mathrm{Fo}_n}{\Omega(1)}}}{\Omega(1)}\left[0.5\Delta\mathrm{Fo}\sum_{j=2}^{n-1}\left(e^{\frac{\mathrm{Fo}_{j-1}}{\Omega(1)}}\times\frac{\delta_{fg}}{k_{fg}}h_f(\mathrm{Fo}_{j-1})(\theta_g(\mathrm{Fo}_{j-1})-\theta_{fg}(1,\mathrm{Fo}_{j-1}))+\right.\right.\\
&\left. e^{\frac{\mathrm{Fo}_j}{\Omega(1)}}\times\frac{\delta_{fg}}{k_{fg}}h_f(\mathrm{Fo}_j)(\theta_g(\mathrm{Fo}_j)-\theta_{fg}(1,\mathrm{Fo}_j))\right)+0.5\Delta\mathrm{Fo}\left(e^{\frac{\mathrm{Fo}_{n-1}}{\Omega(1)}}\times\frac{\delta_{fg}}{k_{fg}}h_f(\mathrm{Fo}_{n-1})(\theta_g(\mathrm{Fo}_{n-1})-\theta_{fg}(1,\mathrm{Fo}_{n-1}))\right.\\
&\left.\left. e^{\frac{\mathrm{Fo}_n}{\Omega(1)}}\times\frac{\delta_{fg}}{k_{fg}}h_f(\mathrm{Fo}_n)(\theta_g(\mathrm{Fo}_n)-\boldsymbol{\theta_{fg}(1,\mathrm{Fo}_n)})\right)\right]
\end{aligned}
\tag{3.10}
$$

Eq. (3.10) allows to solve $\boldsymbol{\theta_{fg}(1,\mathrm{Fo}_n)}$ for each Fo_n step explicitly (knowing all θ values from all Fo_n steps since $\mathrm{Fo}_1 = 0$).

After the calculation of $\theta_{fg}(1,\mathrm{Fo}_n)$, one can solve $\theta_{fg}(\zeta,\mathrm{Fo}_n)$ for other values of ζ using Eq. (3.11).

$$
\begin{aligned}
&\theta_{fg}(\zeta,\mathrm{Fo}_n) = \left(\frac{1}{\mathrm{Bi}}+\zeta\right)\frac{e^{-\frac{\mathrm{Fo}_n}{\Omega(\zeta)}}}{\Omega(\zeta)}\left[0.5\Delta\mathrm{Fo}\sum_{j=2}^{n}\left(e^{\frac{\mathrm{Fo}_{j-1}}{\Omega(\zeta)}}\times\frac{\delta_{fg}}{k_{fg}}h_f(\mathrm{Fo}_{j-1})(\theta_g(\mathrm{Fo}_{j-1})-\theta_{fg}(1,\mathrm{Fo}_{j-1}))+\right.\right.\\
&\left.\left. e^{\frac{\mathrm{Fo}_j}{\Omega(\zeta)}}\times\frac{\delta_{fg}}{k_{fg}}h_f(\mathrm{Fo}_j)(\theta_g(\mathrm{Fo}_j)-\theta_{fg}(1,\mathrm{Fo}_j))\right)\right]
\end{aligned}
\tag{3.11}
$$

For the back side, the discrete version of Eq. (2.28) can be used:

$$
\begin{aligned}
&\theta_{fg}(0,\mathrm{Fo}_n) = \left(\frac{1}{\mathrm{Bi}}+0\right)\frac{1}{\sqrt{\Omega(0)^2-4\mathcal{M}(0)}}\\
&\left[e^{\mathrm{Fo}_n(A+B)}0.5\Delta\mathrm{Fo}\sum_{j=2}^{n}\left(e^{-(A+B)\mathrm{Fo}_{n-1}}\frac{\delta_{fg}}{k_{fg}}h_f(\mathrm{Fo}_{n-1})(\theta_g(\mathrm{Fo}_{n-1})-\theta_{fg}(1,\mathrm{Fo}_{n-1}))+\right.\right.\\
&\left. e^{-(A+B)\mathrm{Fo}_n}\frac{\delta_{fg}}{k_{fg}}h_f(\mathrm{Fo}_n)(\theta_g(\mathrm{Fo}_n)-\theta_{fg}(1,\mathrm{Fo}_n))\right)-\\
&e^{\mathrm{Fo}_n(A-B)}0.5\Delta\mathrm{Fo}\sum_{j=2}^{n}\left(e^{-(A-B)\mathrm{Fo}_{n-1}}\frac{\delta_{fg}}{k_{fg}}h_f(\mathrm{Fo}_{n-1})(\theta_g(\mathrm{Fo}_{n-1})-\theta_{fg}(1,\mathrm{Fo}_{n-1}))+\right.\\
&\left.\left. e^{-(A-B)\mathrm{Fo}_n}\frac{\delta_{fg}}{k_{fg}}h_f(\mathrm{Fo}_n)(\theta_g(\mathrm{Fo}_n)-\theta_{fg}(1,\mathrm{Fo}_n))\right)\right]
\end{aligned}
\tag{3.12}
$$

Chapter 4

Results and Discussion

The purpose of the experiments performed is to validate the model delineated in chapter 2. As an example, one of the experiments produced the following temperature and switch state data (experimental procedure in Appendix B).

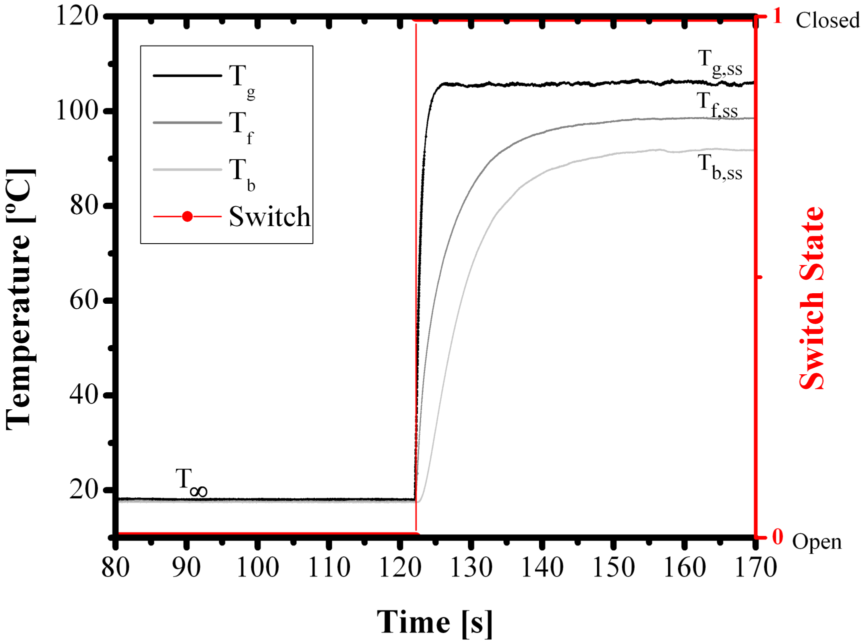

Figure 4.1: Unprocessed experimental data

From the steady state data in Fig. 4.1, one can calculate the steady state convection coefficients using Eqs. (3.3), (3.4) and (3.5) (see Appendix C). The results are $h_{f,ss} = 99.59 \pm 2.38\% \ W \cdot m^{-2}K^{-1}$ and $h_b = 9.94 \pm 2.37\% \ W \cdot m^{-2}K^{-1}$. The front convection coefficient during these procedures will be considered to be constant after the switch closes due to the constant properties of the flow.

Analyzing the data from the thermocouple that measures $T_g(t)$ and the switch, one can conclude that the thermocouple response time is higher than expected for this sudden temperature increase. When the switch is activated the heat gun is already in its final position. Therefore, the hot air should be at steady state temperature when the switch closes. For a more accurate representation of the real hot air temperature, the incident hot air temperature is corrected using the switch information. The resulting incident hot air temperature is shown in Fig. 4.2.

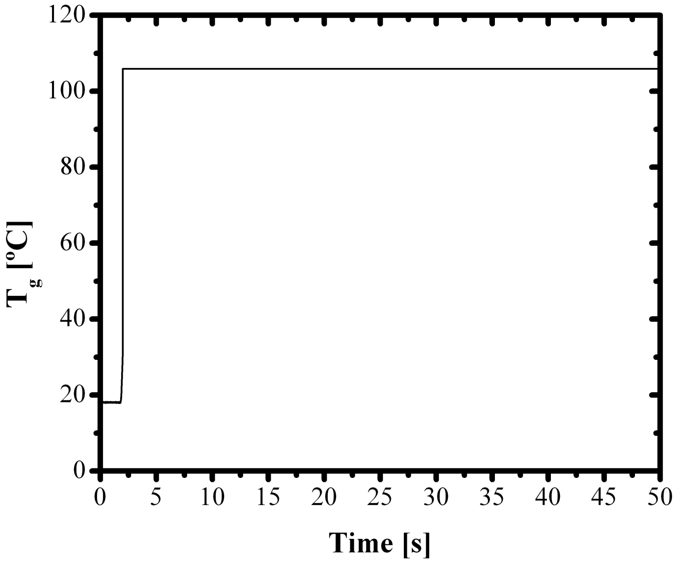

Figure 4.2: Incident hot air temperature.

With that input data, the model generated the results plotted in the graphs of Figs. 4.3 and 4.5.

The graph in Fig. 4.3 compares the experimental temperature evolution of the front side of the barrier against the model predictions considering a possible variation of the specific heat for the thermal barrier between 700 and 900 $J \cdot kg^{-1}K^{-1}$. In general the model predictions are quite accurate. However, at the beginning of the heat exposure, the model underestimates the temperature rise. The error in the model prediction (relative to the total temperature increase) is shown in Fig. 4.4 for all the 10 experimental tests and a $c_{p,fg} = 700\ J \cdot kg^{-1}K^{-1}$.

The graph in Fig. 4.5 does the same comparison but for the back side of the barrier.

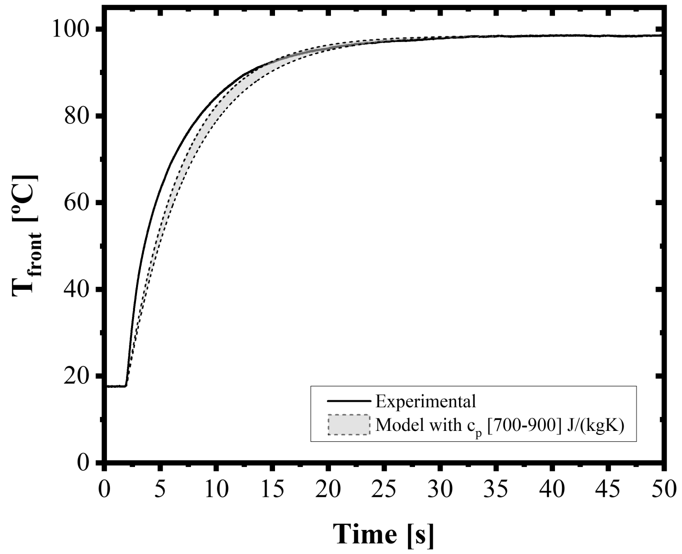

Figure 4.3: Front temperature evolution of the barrier.

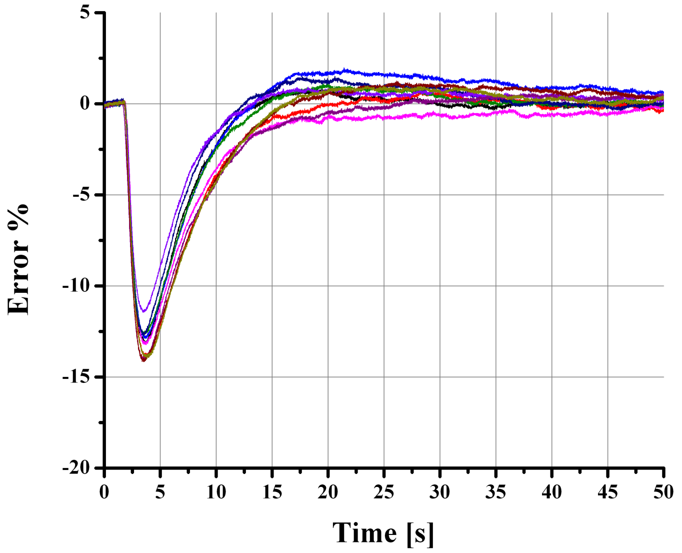

Figure 4.4: Model's prediction error in front side temperature

It should be noted that this solution is calculated using the second order approximation in Eq. (2.28). This prediction also has a good proximity with the experimental values. The error in the model prediction (relative to the total temperature increase) is shown in Fig. 4.4 for all the 10 experimental tests and a $c_{p,fg} = 700\ J \cdot kg^{-1}K^{-1}$.

The graph in Fig. 4.7 shows the evolution of the heat flux entering the front side of the barrier and the heat flux leaving the back side of the barrier.

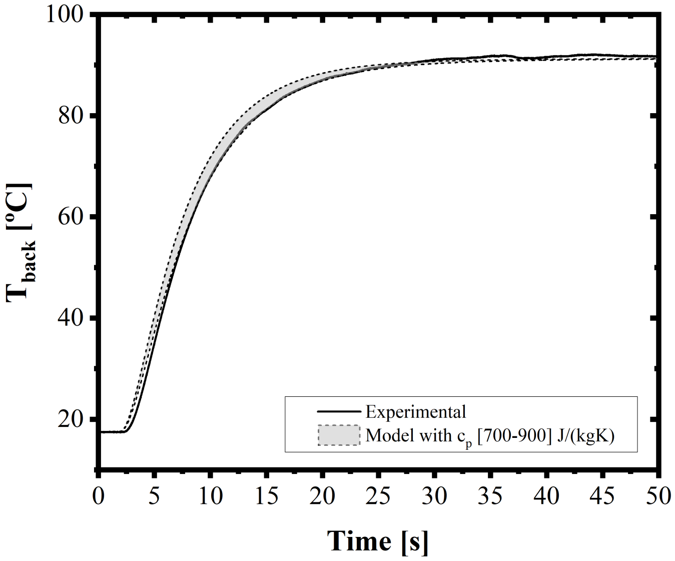

Figure 4.5: Back temperature evolution of the barrier.

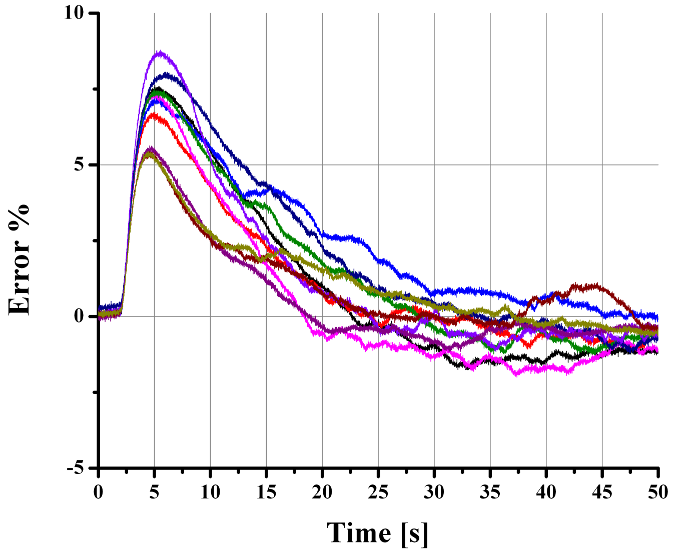

Figure 4.6: Model's prediction error in back side temperature.

This graph is very important because it shows how a thermal barrier achieves its purpose of blocking heat flux.

At the beginning of the exposure, the barrier is at ambient temperature and is subjected to a heat flux spike. However, due to its thermal capacity, the heat flux rejected in the back side only increases slightly.

The temperature on the front side then increases, lowering the heat flux absorbed

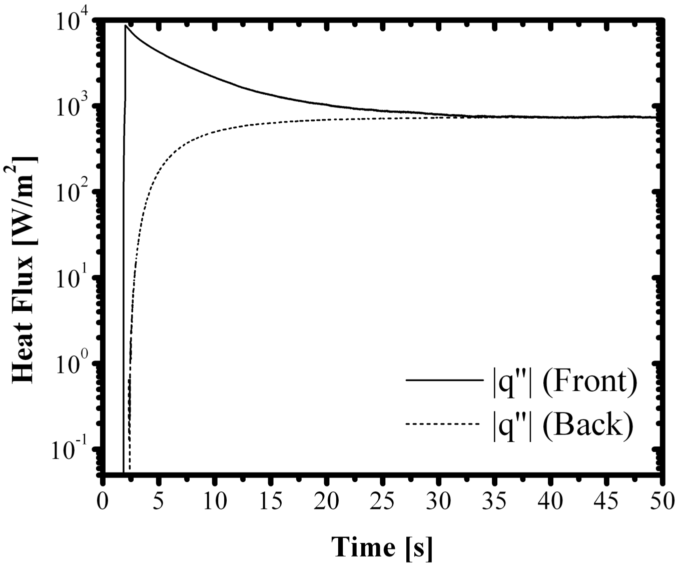

Figure 4.7: Heat flux evolution with time.

by the front side of the barrier. Eventually the barrier cannot store any more energy and the heat flux absorbed equals the heat flux rejected in the back side, as expected when attaining a steady-state condition. In this case, the absorbed heat flux reaches a minimum due to the high temperature of the front side. As the graph shows, the heat flux at steady-state is one order of magnitude lower than the initial heat flux spike, which does not affect the back side of the barrier.

Analyzing the error data from all the experiments one can conclude that the measured front temperature has a faster increase than the model predicts and the measured back temperature has a slower increase than the model. One explanation for this systematic error may be due to a non-negligible contact resistance between the thermocouple membrane and the front aluminium coating, as shown in Fig. 4.8.

While the aluminium foil tape has a very strong adhesive, the thermocouple membrane does not adhere to the barrier's coating. That may cause a temperature difference between the aluminium foil tape and the aluminium coating which the model does not include. Furthermore, the aluminium foil tape might affect the temperature measured by the thermocouple due to the differences in contact resistances in both sides.

In a complex thermal system like this, it is difficult to study the effect that a thermal resistance between the two front aluminium layers might have. This effect will then be studied in a similar but simpler thermal barrier where the fibreglass is a pure thermal

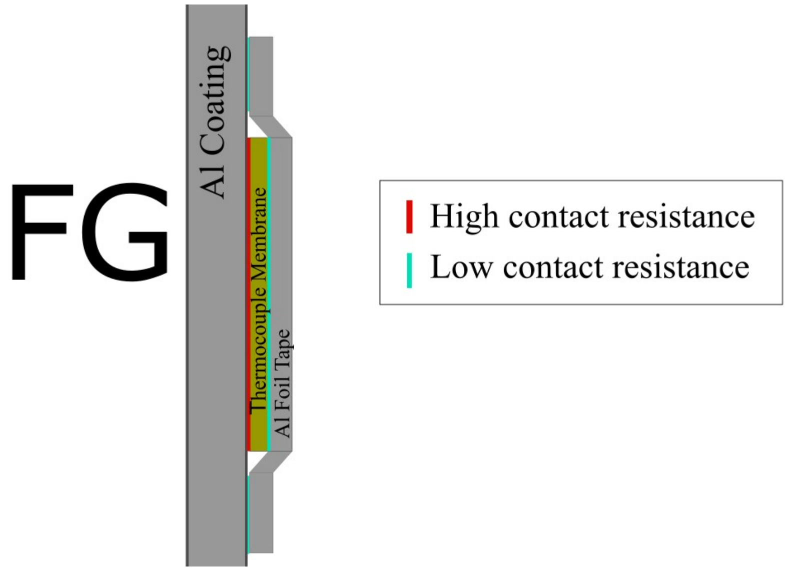
FG
Al Coating
Thermocouple Membrane
Al Foil Tape
High contact resistance
Low contact resistance

Figure 4.8: Simplified representation of the thermocouple installation.

resistance ($c_{p,fg} = 0 \ J \cdot kg^{-1}K^{-1}$).

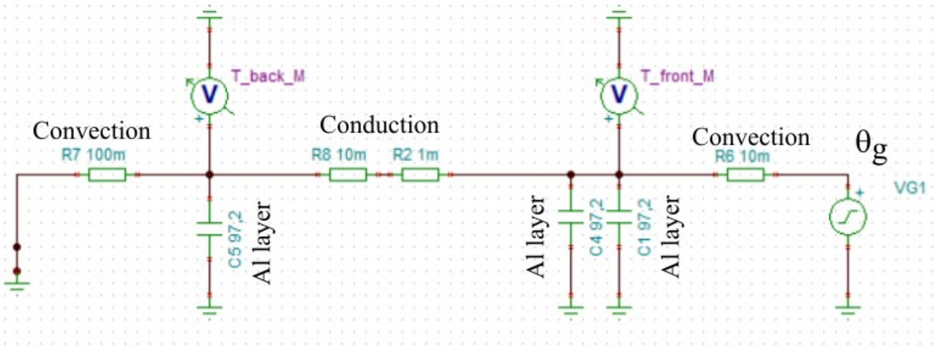
T_back_M
T_front_M
Convection
R7 100m
Conduction
R8 10m
R2 1m
Convection
R6 10m
θ_g
VG1
C5 97.2
Al layer
Al layer
C4 97.2
C1 97.2
Al layer

Figure 4.9: System M electrical analog.

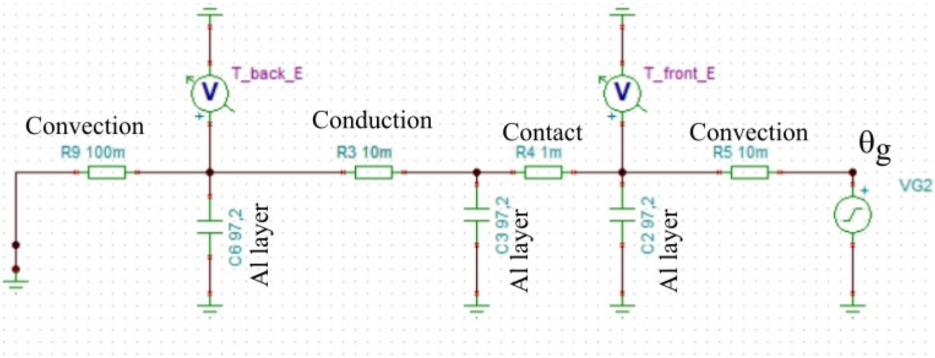
T_back_E
T_front_E
Convection
R9 100m
Conduction
R3 10m
Contact
R4 1m
Convection
R5 10m
θ_g
VG2
C6 97.2
Al layer
C3 97.2
Al layer
C2 97.2
Al layer

Figure 4.10: System E electrical analog.

This simplification will allow to use an electrical-analog method for transient heat flow analysis (as used by Robertson & Gross (1958)) to compare two thermal systems:

- **System M (Fig. 4.9)** where all the barrier's thermal resistance is located in the fibreglass region. This system represents the model,
- **System E (Fig. 4.10)** where 10% of the thermal resistance is located between the front aluminium layers. This system represents the experimental conditions.

The electrical analogy is explained in Table. 4.1.

Table 4.1: Electrical analogy for transient analysis.

Thermal Property	Electrical Analog	Analog Value
Temperature	Voltage	T
Heat flux	Current	q''
Convection	Resistor	$1/h$
Conduction	Resistor	δ/k
Thermal Capacity	Capacitor	$\delta\ \rho\ c_p$

Both systems have the same steady state as all the resistor values are the same. To evaluate the difference in transient behaviour both circuits were simulated and compared in Fig. 4.11.

The results show that the System E has a faster increase in the front side temperature and a slower increase in the back side temperature (relative to System M) due to the resistance between the front aluminium layers. This qualitative behaviour was also observed in the conducted experiments. Therefore, it is reasonable to conclude that the contact resistance in the front side of the barrier may be skewing the measured temperature evolution.

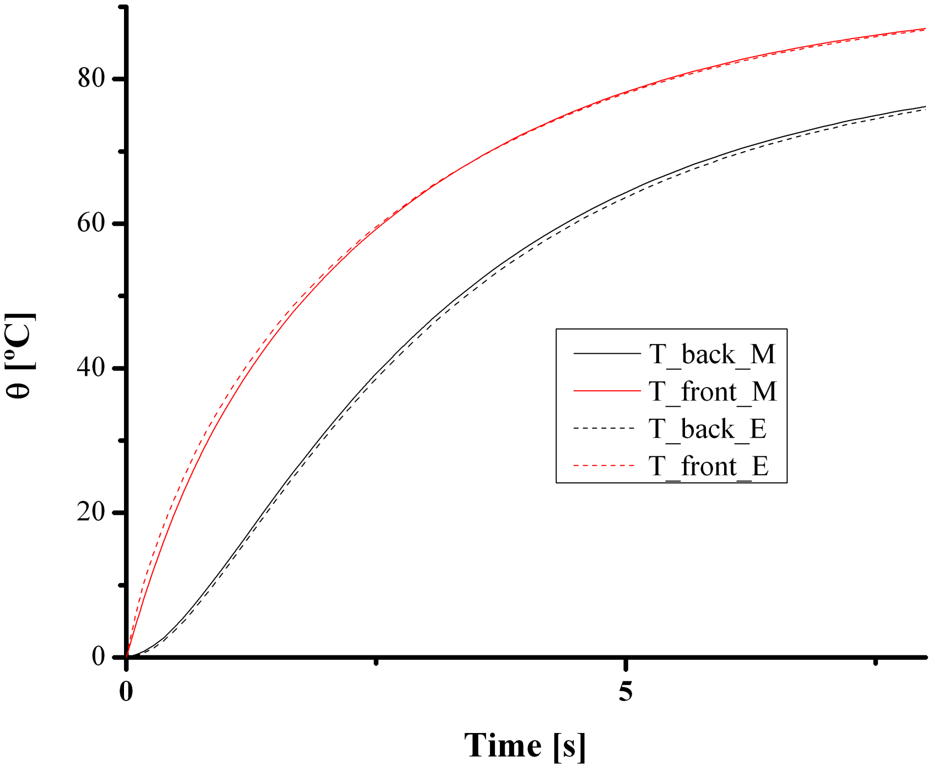

Figure 4.11: Simulated temperature evolution.

Chapter 5

Conclusions

The optimization of fireproof thermal barriers requires the ability to accurately model the heat transfer between a fire front and a thermal barrier. Most models consider metallic barriers, and the application of a lumped-capacity approach to predict its thermal behaviour. However, previously reported experiments show the inadequacy of this approach to the heat transfer modeling of the thermal barrier under research made of a fiberglass tissue coated with an aluminium thin layer. Therefore, this work introduces a simple analytical model developed for a flat plate with two layers of disparate materials and geometries. Namely, one thicker layer with low thermal conductivity, and a thinner layer of a high thermally conductive and reflective (in radiation terms) material. This scheme is the general case of the aluminium coated fibreglass thermal barrier exposed to a heat flux under research.

The model departs from the uni-dimensional heat equation with a convective boundary condition on the back side (cold side) and an arbitrary and transient heat flux on the front side. Due to the complexity of this problem, one can only delineate an approximate analytical solution, which, in the present case, uses a Padé Approximant. The comparison between the approximate analytical solution and a numerical reference solution, using finite-differences, revealed promising results.

To validate the model, simple laboratory setup allowed to conduct experiments under transient heat transfer conditions using a convective heat source on the front side. The experiments focused on creating a step variation in the heat flux because the theoretical testing indicated the model would produce worse results in fast changing heat fluxes.

Comparing the model predictions with the measured temperature evolution of both sides of the barrier revealed that the model is generally accurate.

Future work

This project seeks ultimately to develop an active water-cooled fire-proof barrier to withstand higher heat fluxes for large amounts of time while preserving its integrity. Therefore, this model should be improved in order to included water cooling mechanisms in the barrier. The improved model would allow optimizing the preservation of the thermal barrier while consuming as little water as possible.

Bibliography

Batista, Rui Marcelo. 2018. *Mechanisms for Active Protection of People and Infrastructures against Forest Fires.* M.Phil. thesis, Universidade de Coimbra.

Hernández, Lourdes. 2019. *The Mediterranean burns.* Tech. rept. World Wildlife Fund.

Hsu, Sheng-Yen, T'ien, James, Takahashi, Fumiaki, & Olson, Sandra. 2011. Modeling Heat Transfer in Thin Fire Blanket Materials under High External Heat Fluxes. *Fire Safety Science*, **10**(06), 973–986.

Incropera, Frank P. 2006. *Fundamentals of Heat and Mass Transfer.* Hoboken, NJ, USA: John Wiley & Sons, Inc.

Lev, Y., & Strachan, D. C. 1989. A study of cooling water requirements for the protection of metal surfaces against thermal radiation. *Fire Technology*, **25**(3), 213–229.

Meredith, Karl, de Vries, Jaap, Wang, Yi, & Xin, Yibing. 2013. A comprehensive model for simulating the interaction of water with solid surfaces in fire suppression environments. *Proceedings of the Combustion Institute*, **34**(12), 2719–2726.

Redmond, M., & Mastropietro, A. 2015. Thermophysical and Optical Properties of Materials Considered for Use on the LDSD Test Vehicle.

Robertson, A. F., & Gross, Daniel. 1958. An Electrical-Analog Method for Transient Heat-Flow Analysis. *Journal of Research of the National Bureau of Standards*, **61**(2).

Appendix A: Change in system response due to transfer function approximations

To evaluate the hypothesis in the paper, it is simpler to study a simpler transfer function of a general first order system $F(s)$ with amplification K and time constant τ.

$$F(s) = \frac{K}{\tau s + 1} \tag{1}$$

This simple transfer function will allow to study the effects that different approximations in the Laplace domain have in the system response. Two types of approximations are analysed: L and $H(s)$.

For small absolute values of s, $F_{1sOS}(s \to 0) \approx K = L$ while higher absolute values of s approximate $F_{1sOS}(s \gg 1) \approx \frac{K}{\tau s} = H(s)$. All transfer functions are represented in Fig. 1

The following step is to analyze the response ($r(t)$) of each transfer function for two types of inputs: 1) a step function and 2) ramp function. The ramp input function allows to evaluate if the approximations in the Laplace domain affects the accuracy of the response in different time scales, or in different regimes (transient or steady-state). It is a viable assessment because, even for large time scales, a ramp input function does not achieve the steady state. The resulting response functions are represented in Fig. 2 and 3.

It can be seen from the step function responses that the high absolute s value approximation ($H(s)$) represents accurately the response for only small values of time. It can also be seen that the low absolute s value approximation (L) represents accurately

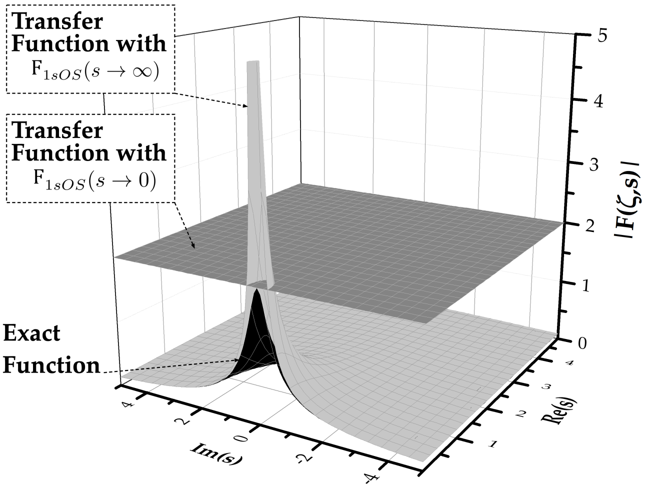

Figure 1: Exact transfer function (black), $F_{1sOS}(s \to 0)$ transfer function (dark grey) and $F_{1sOS}(s \to \infty)$ transfer function (light grey) (For $K = 2$ and $\tau = 3$).

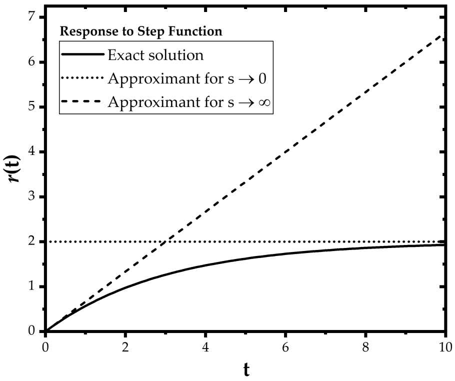

Figure 2: Response to a unitary step input function for all transfer functions (For K=2 and $\tau = 3$).

the response for higher values of time or the steady-state.

From the ramp input function, it can be seen again that the $H(s)$ approximation is only accurate for low values of time. It shows also that L approximation is never accurate, because the steady state is never achieved. However, this is the approximation that has a similar shape to the exact function for higher values of time, which is required in the thermal barrier.

From this study, it is reasonable to conclude that the approximation in the Laplace domain will have to be focused around the origin of the complex plane (even though

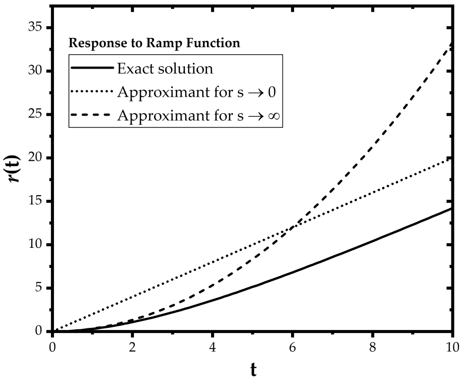

Figure 3: Response to a ramp input function (slope=1) for all transfer functions (For K=2 and $\tau = 3$).

this study analysed a different transfer function).

Apendix B: Experimental Procedures

Procedure to determine the barrier's thermal conductivity:

1. Begin data acquisition.
2. Turn on heat gun in the 100°C setting at medium fan speed.
3. Wait 2-3 minutes to reach steady state.
4. Stop data acquisition.
5. Turn off heat gun.
6. Let the barrier reach ambient temperature until next procedure.

Procedure to measure barrier response to convective heat flux:

1. Begin data acquisition.
2. Rotate the heat gun 60° upwards.
3. Turn on heat gun in the 100°C setting at medium fan speed.
4. Wait 1 minute to reach steady state.
5. Drop the heat gun in a fast motion.
6. Wait 2 minutes to reach steady state

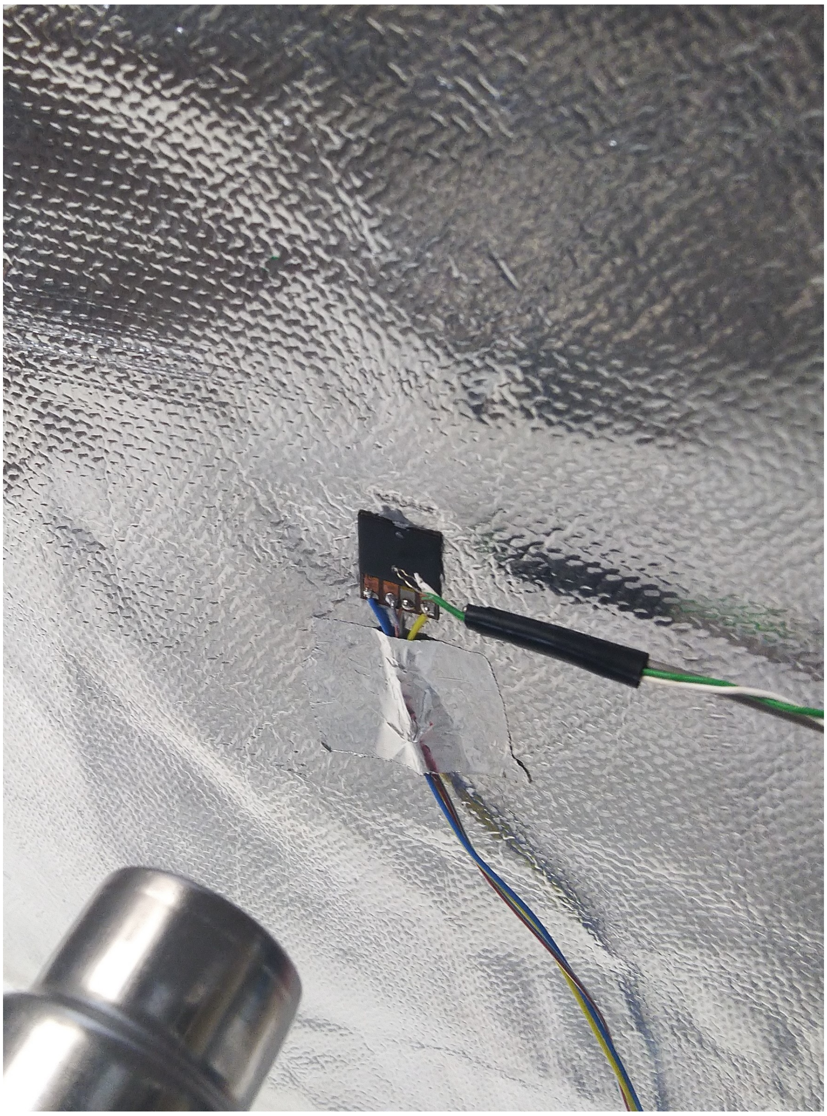

Figure 4: Front-side of barrier

7. Stop data acquisition.

8. Turn off heat gun.

9. Let the barrier reach ambient temperature until next procedure.

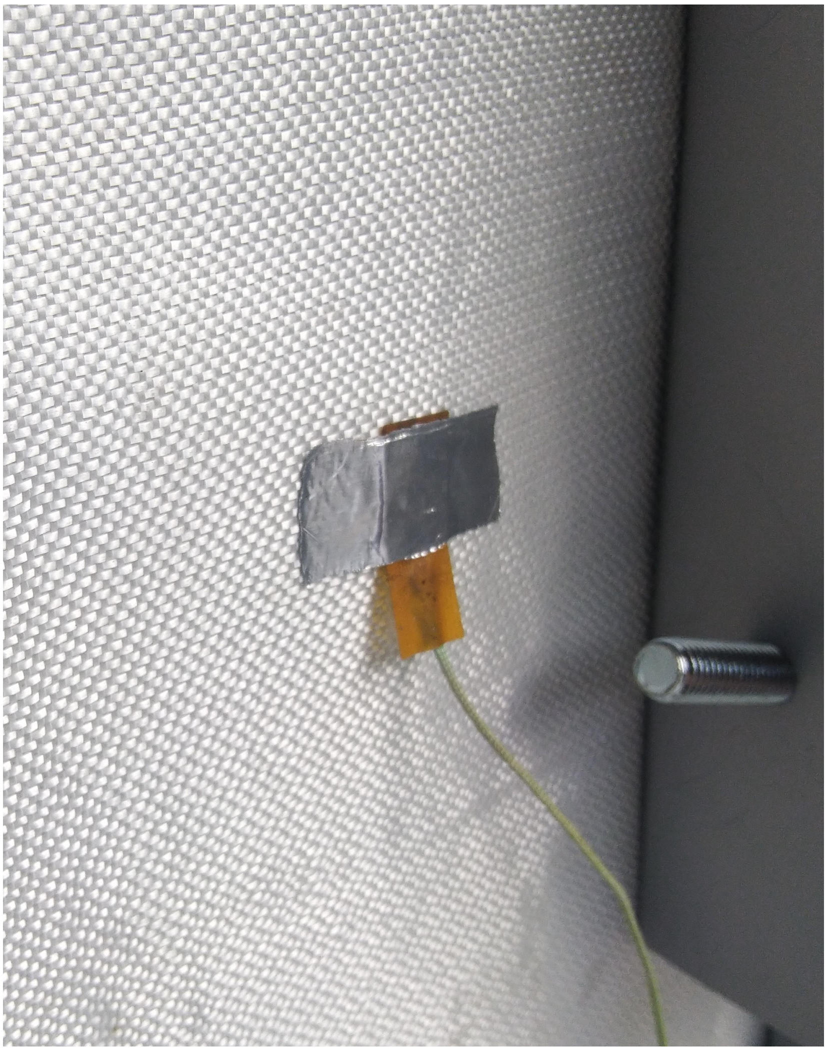

Figure 5: Back side of barrier

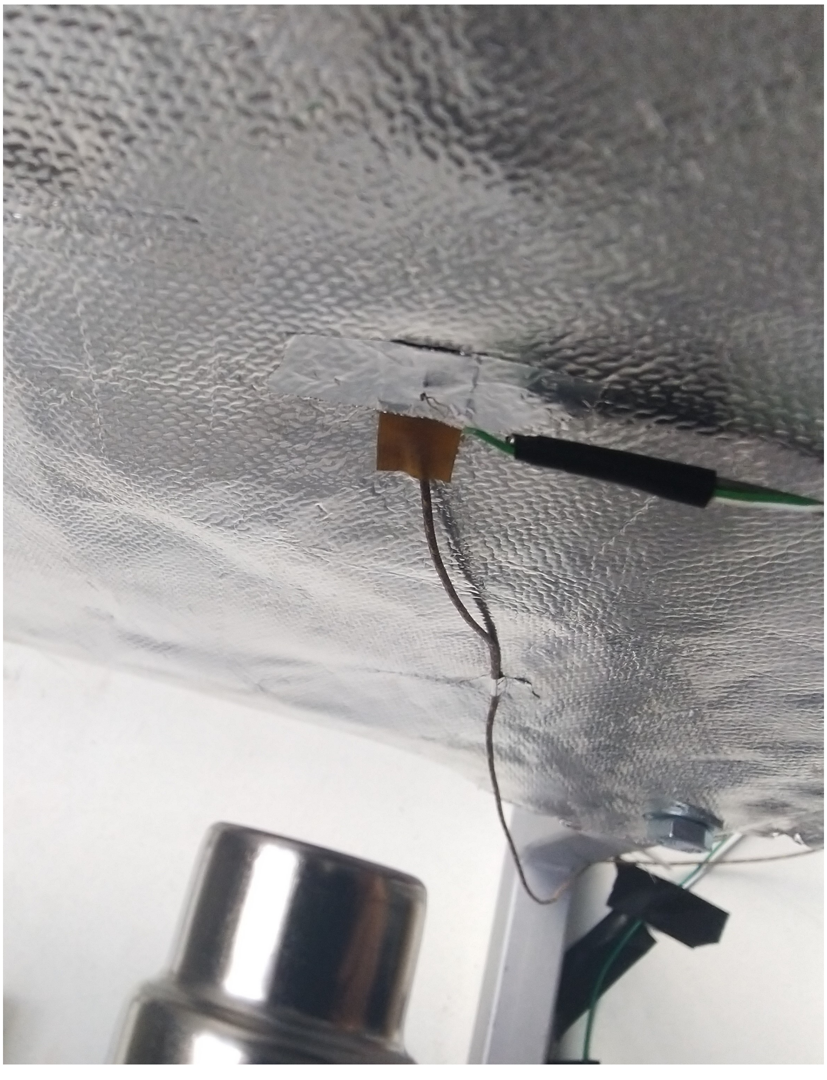

Figure 6: Front side of barrier

Apendix C: Uncertainty calculations

Uncertainty of k_fg:

Using measurements from 6 different experiments, a total sample size of $N = 6000$ values of $q''_{a,c}$, T_f and T_b were used to calculate the average of k_{fg}/δ_{fg}:

$$\frac{k_{fg}}{\delta_{fg}} = \frac{q''_{a,c}}{T_f - T_b} \tag{2}$$

$$\overline{\left(\frac{k_{fg}}{\delta_{fg}}\right)} = 110.51\ W \cdot m^{-2}K^{-1} \tag{3}$$

The statistical uncertainty of this mean, within a 95% confidence level, is given by $\epsilon_{k_{fg}/\delta_{fg}} = 1.96\frac{s_{k_{fg}/\delta_{fg}}}{\sqrt{N}}$, where $s_{k_{fg}/\delta_{fg}}$ is the standard deviation of measured values, resulting in ± 0.1667 $[W \cdot m^{-2}K^{-1}]$.

To calculate the average of k_{fg}:

$$k_{fg} = \left(\frac{k_{fg}}{\delta_{fg}}\right)\delta_{fg} \tag{4}$$

$$\overline{k_{fg}} = 0.03315\ W \cdot m^{-1}K^{-1} \tag{5}$$

The calculation of the uncertainty of k_fg requires the use of the propagation of error equation. The uncertainty of the caliper is considered to be half the resolution of the scale.

$$\epsilon_{k_{fg}} = \sqrt{\left(\left(\frac{k_{fg}}{\delta_{fg}}\right) \times \epsilon_{\delta_{fg}}\right)^2 + (\delta_{fg} \times \epsilon_{k_{fg}/\delta_{fg}})^2} \tag{6}$$

$$\epsilon_{k_{fg}} = 5.55 \times 10^{-4}\ W \cdot m^{-1}K^{-1} \tag{7}$$

In conclusion:

$$k_{fg} = 0.03315 \pm 1.67\%\ W \cdot m^{-1}K^{-1} \tag{8}$$

Uncertainty of T_∞:

The ambient temperature is calculated from a sample of $N = 300$ values measured in the back side of the barrier before the exposure begins.

$$\overline{T_\infty} = 17.55°C \tag{9}$$

The uncertainty is given by:

$$\epsilon_{T_\infty} = 1.96\frac{s_{T_\infty}}{\sqrt{N}} \tag{10}$$

$$\epsilon_{T_\infty} = 0.0040°C \tag{11}$$

In conclusion:

$$T_\infty = 17.55 \pm 0.02\%\ W \cdot m^{-1}K^{-1} \tag{12}$$

Uncertainty of h_f

The general formula is given by:

$$h_f = k_{fg} \times \frac{1}{\delta_{fg}} \times \frac{T_f - T_b}{T_g - T_f} \tag{13}$$

Using $N = 300$ samples of $\frac{T_f-T_b}{T_g-T_f}$ and previously calculated values, the average is:

$$\overline{h_f} = 99.59\ Wm^{-2}K^{-1} \tag{14}$$

The uncertainty is calculated using the propagation of error:

$$\epsilon_{h_f} = \sqrt{\left(\frac{T_f - T_b}{T_g - T_f}\frac{1}{\delta_{fg}}\epsilon_{k_{fg}}\right)^2 + \left(\frac{k_{fg}}{\delta_{fg}}\epsilon_{\frac{T_f-T_b}{T_g-T_f}}\right)^2 + \left(k_{fg} \times -\frac{1}{\delta_{fg}^2} \times \frac{T_f - T_b}{T_g - T_f}\epsilon_{\delta_{fg}}\right)^2} \tag{15}$$

$$\epsilon_{h_f} = 2.37\ Wm^{-2}K^{-1} \tag{16}$$

In conclusion:

$$h_f = 99.59 \pm 2.38\% \; W \cdot m^{-2}K^{-1} \tag{17}$$

Uncertainty of h_b

The general formula is given by:

$$h_f = k_{fg} \times \frac{1}{\delta_{fg}} \times \frac{T_f - T_b}{T_b - T_\infty} \tag{18}$$

Using $N = 300$ samples of $\frac{T_f - T_b}{T_b - T_\infty}$ and previously calculated values, the average is:

$$\overline{h_b} = 9.94 \; Wm^{-2}K^{-1} \tag{19}$$

The uncertainty is calculated using the propagation of error:

$$\epsilon_{h_f} = \sqrt{\left(\frac{T_f - T_b}{T_b - T_\infty}\frac{1}{\delta_{fg}}\epsilon_{k_{fg}}\right)^2 + \left(\frac{k_{fg}}{\delta_{fg}}\epsilon_{\frac{T_f - T_b}{T_b - T_\infty}}\right)^2 + \left(k_{fg} \times -\frac{1}{\delta_{fg}^2} \times \frac{T_f - T_b}{T_b - T_\infty}\epsilon_{\delta_{fg}}\right)^2} \tag{20}$$

$$\epsilon_{h_b} = 0.236 \; Wm^{-2}K^{-1} \tag{21}$$

In conclusion:

$$h_b = 9.94 \pm 2.37\% \; W \cdot m^{-2}K^{-1} \tag{22}$$